Explosive cytotoxicity of 'ruptoblasts' bridges hormonal surveillance and immune defense

Chew Chai[1], Eliya Sultan[2], Souradeep R. Sarkar[1], Lihan Zhong[1], Dania Nanes Sarfati[3], Orly Gershoni-Yahalom[2], Christine Jacobs-Wagner[3,4,5], Benyamin Rosental[2,*], Bo Wang[1,6,*]

[1]Department of Bioengineering, Stanford University, Stanford CA, USA

[2]The Shraga Segal Department of Microbiology, Immunology, and Genetics, Faculty of Health Sciences, Center for Regenerative Medicine and Stem Cells, Ben Gurion University of the Negev, Beer Sheva, Israel

[3]Department of Biology, Stanford University, Stanford CA, USA

[4]Department of Microbiology and Immunology, Stanford University, Stanford CA, USA

[5]Howard Hughes Medical Institute, Stanford University, Stanford CA, USA

[6]Department of Developmental Biology, Stanford University School of Medicine, Stanford CA, USA

*Correspondence should be addressed to B.R. (rosentab@post.bgu.ac.il) or B.W. (wangbo@stanford.edu)

Abstract:

Cytotoxic killing is an essential immune function, yet its cellular mechanisms have been characterized in only a few model species. Here, we show that planarian flatworms harness a unique cytotoxic strategy. In planarians, activin, a hormone regulating regeneration and reproduction, also acts as an inflammatory cytokine. Overactivation of activin signaling – through protein injection, genetic chimerism, or bacterial infection – triggers 'ruptoblasts', an undocumented immune cell type, to undergo 'ruptosis', a unique mode of cell bursting that eliminates nearby cells and bacteria in mere minutes, representing one of the fastest cytotoxic mechanisms observed. Ablating ruptoblasts suppresses inflammation but compromises bacterial clearance, highlighting ruptoblasts' broad-spectrum immune functions. We further identified ruptoblast-like cells in diverse basal bilaterians, unveiling an alternative strategy that couples hormonal regulation with immune defense and expanding the landscape of evolutionary immune innovations.

Main:

The animal kingdom is replete with diverse immune strategies, yet much of our mechanistic understanding derives from a handful of well-characterized model organisms. While basic immune functions, such as pathogen clearance, damage control, and recognition of non-self or malfunctioning cells, are conceivably widespread (*1-3*), whether more advanced functions, like those associated with mammalian adaptive immunity, exist in basal animals remains mostly unclear (*4-6*). This knowledge gap prompted us to explore whether animals lacking adaptive immunity might have evolved alternative cell types and pathways to achieve analogous functions, which may help discover novel immune mechanisms with unique advantages.

We considered a function of cytotoxic T cells: maintaining hormonal homeostasis by eliminating cells that produce hormones at abnormally high levels – a complex process that requires precise recognition of autoantigens and quantitative interpretation of their concentrations (**Fig. 1A**) (*7*). This function is particularly crucial in proliferative tissues, such as the pancreas, thyroid, and adrenal gland, where continuous cell division increases the risk of mutations that can lead to hypersecreting clones (*8*). The mammalian strategy, however, has two major limitations. First, since the autoantigens are typically produced during hormone biosynthesis and secretion, T cells predominantly target differentiated hormone-secreting cell types, such as β-cells (*9*), leaving stem cell populations that may harbor or propagate mutations largely unchecked. Second, sustained activation of memory T cells can lead to prolonged cytotoxicity and autoimmune disorders (*10, 11*). For example, while immune surveillance of the insulin pathway can avert life-threatening conditions like hyperinsulinemia, it may also inadvertently destroy healthy cells, potentially causing type I diabetes.

Here our study of the planarian flatworm *Schmidtea mediterranea* reveals a novel strategy that can overcome these limitations, providing both broader efficacy and reduced risk of autoimmunity. Planarians can reproduce through fission and regenerate all missing body parts using a large pool of somatic stem cells, known as neoblasts (*12-14*). Neoblasts divide every couple of days to sustain the stem cell pool and replenish all differentiated tissues, even during tissue homeostasis, but this extensive proliferation increases the risk of somatic mutations that can lead to hormonal dysregulation just like in mammalian organs such as the pancreas.

In planarians, regeneration, reproduction, and tissue homeostasis are all regulated by activin, a hormone whose level must be finely tuned and stably maintained: excessive activin can impair regeneration (*15-17*), while insufficient levels hinder both fission (*18*) and sexual reproduction (**fig. S1**). We found that activin acts as a potent inflammatory cytokine in planarians, directly linking hormonal regulation with immune responses. When activin becomes excessive, a unique immune cell type, 'ruptoblasts', are triggered to undergo a rapid, sacrificial cytotoxic process, 'ruptosis', eradicating nearby cells in a singular, explosive event (**Fig. 1B**). Although ruptosis involves the release of granular contents in a manner reminiscent of neutrophil and mast cell degranulation (*19, 20*), it is distinct from any previously described cytotoxic or cell death processes (**table S1**). Ruptosis is spatially restricted and specifically induced by activin, rather than by conventional immune stimuli such as pathogens, but this mode of specificity allows them to eliminate activin-secreting cells, neoblasts, and microbes at once, thereby addressing the shortcomings of T cells' sequential, contact-dependent killing (*21, 22*) that is limited to fully differentiated hormone secreting cells. Moreover, the one-off nature of ruptosis prevents prolonged immune activation, minimizing collateral damage and autoimmunity.

Importantly, our analyses also suggest that ruptoblast-like cells are conserved from the base of the bilaterian tree. Single-cell datasets from diverse animals (*23–25*) reveal cell types with similar gene expression signatures, which have been overlooked due to their lack of canonical immune markers. Our findings thus uncover a previously unknown immune cell type with broad-spectrum activity, demonstrating how animals can evolve innovative strategies that rival, and in some ways surpass, the functions of adaptive immune cells.

Activin-induced inflammatory responses

To test whether excess activin is sufficient to trigger inflammation, we generated recombinant proteins for ACT-2, one of the two planarian activin homologs (*15*). We injected planarians (CIW4 asexual clonal line) with either ACT-2 or control proteins (human CD8A and Activin-B), and used Western blotting to measure phosphorylated Smad2/3 (p-Smad2/3), the canonical effector of activin signaling. As expected, p-Smad2/3 levels increased only in ACT-2 injected animals (**Fig. 1C, fig. S2A**), confirming the functionality and specificity of our recombinant proteins.

We then examined whether the p38 pathway was activated by activin as a conserved inflammatory response, which was previously shown to drive tissue degeneration during bacterial and fungal infection in planarians (*26*, *27*). Indeed, only in ACT-2 injected planarians did we detect elevated phosphorylation of p38-1 (p-p38-1) (**Fig. 1C, fig. S2B-C**). Knockdown of *act-2* or activin receptors, drastically reduced both p-Smad2/3 and p-p38-1 levels during either homeostasis or after ACT-2 injection (**Fig. 1D, fig. S2D-F**), further confirming that *p38-1* acts downstream of activin. Phenotypically, ACT-2 induced excessive cell death at the injection sites,

quantified by TUNEL assay, as well as tissue lesions, both of which were alleviated by RNA interference (RNAi) against *p38-1* (**Fig. 1E, fig. S2G**). These data suggest that excess activin triggers a p38-mediated inflammatory response, establishing a direct link between hormonal dysregulation and immune activation.

Activin as an inflammatory cytokine in genetic chimeras

Since ACT-2-induced lesions resolved within 24 hr, presumably due to degradation or clearance of the recombinant proteins (*28*), we sought a method to sustain activin overactivation. Drawing inspiration from classic experiments fusing distinct planarian species (*29*), we wondered whether this approach could provoke immune rejection analogous to that commonly observed in mammalian organ transplant. We optimized a protocol (*30*) to generate genetic chimeras by fusing asexual (A) and sexual (S) *S. mediterranea* along the midline (**Fig. 2A, fig. S3A-B**). Despite seemingly complete tissue integration – such as shared anterior and posterior poles and midline, integrated muscle networks, nervous system, gut branches, and a single pharynx (**Fig. 2B**, **fig. S3C-D**) – these genetic chimeras exhibited three key pathological features, indicative of a chronic inflammatory response to incompatible genotypes.

First, the two genotypes remained segregated, as measured by PCR-RFLP genotyping (*31*) (**Fig. 2C**) and the distribution of strain-specific RNA virus (SmedTV) (*32*) at 20 days post fusion (dpf) (**Fig. 2D**). This indicated a rejection between the two genotypes, as neoblasts and/or postmitotic progenitors are thought to have significant migratory capacity (*33*). Second, unlike homotypic fusions, the chimeras failed to feed, a trait typically associated with severely sick animals. Finally, ~40% of chimeras developed lesions at the fusion site by ~14 dpf, progressing to whole-

body disintegration within a day (**Fig. 2E**). This pathology resembled the phenotype induced by ACT-2 protein injections.

To investigate if these lesions stemmed from activin overactivation, we measured p-Smad2/3 (**Fig. 2F**) and p-p38-1 (**Fig. 2G**) in chimeras and observed markedly increased levels of both. Knocking down *p38-1* prior to fusion prevented these lesions, establishing a causal link between molecular inflammatory responses with the lesion phenotype (**Fig. 2H**). We next asked whether inflammation was systemic or confined to the midline, where the two genotypes interacted. RNAseq of both midline tissues and whole chimeras (with and without lesions) revealed that genes downregulated after *act-2* RNAi (*15*) were globally upregulated relative to simple averages of homotypic fusions, especially in animals with lesions (**Fig. 2I**), suggesting a body wide inflammatory response. Together, our results demonstrate that genetic chimerism induces chronic inflammation, with activin serving as a general inflammatory cytokine.

Ruptoblasts and ruptosis

To identify the cell type driving the inflammatory responses to activin, we dissociated planarians into single cell suspension and monitored their responses to ACT-2 *ex vivo*. Strikingly, a subset of cells underwent explosive lysis within ~5 min, whereas control proteins had minimal effects (**fig. S4A, movie S1**). Flow cytometry analysis confirmed activin-induced lysis in a dose-dependent manner (**Fig. 3A**), regardless of the planarian genotype (**fig. S4B**). Thus, ACT-2 itself, rather than allogeneic response to non-self cells, is sufficient to trigger this special form of lysis. This also suggests that the cells recognizing non-self genotypes (and possibly producing activin)

are distinct from the cells that execute the lysis, and that proximity between these cell populations is necessary for the *in vivo* killing observed in chimeras.

Consistently, p-p38-1 level increased rapidly within 3 min of ACT-2 treatment, in a concentration-dependent manner, before lysis occurred (**Fig. 3B, fig. S4C**). In addition, cytoskeleton inhibitors reduced lysis (**fig. S4D**), highlighting the importance of cytoskeleton remodeling, a key process in many immune responses (*34*, *35*).

We next developed a fluorescence activated cell sorting (FACS) strategy to enrich these explosive cells. Based on morphology, we first gated for high-granularity cells (**fig. S5A**), then subdivided by cell size and a cytoplasmic stain (Calcein Ultrablue) (**Fig. 3C**). Testing each subpopulation's response to ACT-2, we identified a single population (P5) that activated p38 (**Fig. 3D**). A major fraction (~60-70%) of these cells burst upon adding activin releasing a large amount of granules. These granules dispersed and disappeared entirely within 2 min (**Fig. 3E, fig. S5B, movie S2-3**). We refer to this explosive cell death as 'ruptosis' and these cells as 'ruptoblasts'.

To visualize their killing process, we labeled P5 cells with CellTrace Violet and co-incubated them with unlabeled P5-depleted cell fractions. Upon inducing ruptosis with ACT-2, cells near the ruptoblasts were killed as indicated by propidium iodide (PI) staining (**Fig. 3F, movie S4**). Notably, ruptoblasts neither released extracellular DNA traps, as widely studied in neutrophils (*36*), nor engaged in direct contact with the target cells, like T cells or natural killer (NK) cells would (*21*, *37*). Instead, they appeared to release diffusive cytotoxic agents upon ruptosis.

To determine the molecular identity of ruptoblasts, we performed single-cell RNAseq on sorted P5 cells briefly treated with either control (CD8A) or ACT-2 proteins (**Fig. 3G**). Under this condition, we anticipated ruptoblasts to be selectively depleted in the ACT-2-treated sample before widespread killing occurred. Indeed, three cell clusters (11, 13 and 15) were most depleted among the 16 transcriptomically distinct populations (**Fig. 3H, fig. S6A**). These three clusters expressed high levels of *actR1* and *p38-1* but not *act-2*, implicating that they only sense and respond to activin without amplifying it via activin secretion (**Fig. 3I**). Based on known marker genes (*38*) (**Fig. 3I, fig. S6A-B**), clusters 11 and 13 were annotated as parenchymal glandular cells, while cluster 15 were *cathepsin*$^+$ phagocytic cells (*39*).

To verify which cluster is responsible for ACT-2-induced cytotoxicity *in vivo*, we selectively ablated each of the three clusters using RNAi against their specific transcription factors (TFs) (**Fig. 4A-B, fig. S6C**) and then tested whether these treatments eliminated ACT-2-induced cell death. Only animals treated with *fer3l-1* RNAi, which depleted cluster 11, exhibited a significant reduction in cell death near the ACT-2 injection site (**Fig. 4C, fig. S6D**), along with diminished p38 activation (**Fig. 4D**). In contrast, depletion of clusters 13 and 15 via RNAi targeting their respective TFs, *nkx2l* and *ets-1* (**Fig. 3I, 4C**), had no such effect. These findings identified cluster 11 as ruptoblasts and the primary responders to ACT-2 *in vivo*. Surprisingly, *cathepsin*$^+$ cells (cluster 15), previously thought to be presumptive immune cells in planarians due to their capacity to engulf bacteria (*39*) and the expression of many immune-related genes (**Fig. 3I**), such as homologs of mammalian neutrophil markers, myeloperoxidase (*mpo*) (*40*) and neutrophil elastase (*ne*) – granular enzymes essential for chromatin decondensation and formation of

extracellular traps (*41*) – were not responsible for the observed cytotoxicity under these conditions.

In vivo cytotoxicity of ruptoblasts

Ruptoblasts are broadly distributed throughout the planarian body, except in the head region (**Fig. 4A**). Injecting ACT-2 proteins eliminated ruptoblasts at the injection site, along with nearby activin-secreting cells and neoblasts within ~100 μm (**Fig. 4E, fig. S6E**). The lost ruptoblasts were quickly replenished by neoblasts, as shown by bromodeoxyuridine (BrdU) pulse-chase experiments (**Fig. 4F, fig. S6F**). This continuous replenishment is key for sustaining ruptoblast population and function.

In chimeras, we observed that ruptoblast density sharply declined throughout the body (**Fig. 4G-H**), consistent with the *ex vivo* observations where both the asexual and sexual cells lysed similarly upon ACT-2 activation (**fig. S4B**). Surprisingly, in surviving chimeras by 21 dpf, ruptoblasts rebounded in sexual tissues, potentially reflecting distinct steady states of the two genotypes under high activin. Finally, eliminating ruptoblasts via *fer3l-1* RNAi before fusion prevented lysis (**Fig. 4I**) and reduced p38-1 activity (**Fig. 4J**), confirming that ruptoblasts are central to the destructive inflammation triggered by prolonged activin elevation.

Bacterial clearance by ruptoblasts

Given that many cytotoxic cells can eliminate both aberrant cells and pathogens, we hypothesized that ruptoblast-mediated cytotoxicity might be also activated during bacterial infections. To explore this, we challenged planarians with varying concentrations of pathogenic

Pseudomonas (**Fig. 5A**) (*26*). Bacterial infection indeed activated the activin pathway, as measured by p-Smad2/3, but only above a specific bacterial load (**Fig. 5B, fig. S7A**). Additionally, ACT-2 enhanced bacterial engulfment by planarian cells, without affecting pinocytosis (**fig. S7B-C**), again demonstrating its role as a cytokine. Strikingly, not only *act-2* RNAi but also *fer3l-1* RNAi prior to infection increased animals' sensitivity to bacterial challenge; these animals lysed days ahead of controls (**Fig. 5C**). The timing of lysis closely mirrored that of animals exposed to higher bacterial loads (**Fig. 5A**), suggesting that infection-induced activin may activate ruptoblasts to assist in bacterial clearance. Consistently, these 'immune compromised' animals exhibited significantly higher commensal bacterial loads compared to controls (**Fig. 5D**).

This prompted us to investigate whether ruptoblasts can directly kill bacteria. Remarkably, incubation of P5 cells with GFP-expressing *E. coli* did not induce ruptosis or bacterial death, suggesting that ruptoblasts did not sense bacteria unlike typical immune cells (*42*, *43*). However, upon adding ACT-2, ruptoblasts began to rupture within ~5 min, and ~ 3 min after that, the nearby bacteria lost GFP signal, indicative of membrane leakage, and ultimately took up PI (**Fig. 5E-F, movie S5**). About 45% of bacterial cells surrounding the ruptoblasts were killed in a single explosion, and the abrupt loss of GFP implied that the killing agents are highly potent. Notably, we did not observe ruptoblasts engulfing bacteria, consistent with prior studies showing that planarian phagocytic cells are *cathepsin*$^+$ (*39*). Since *cathepsin*$^+$ cells also express *act-2* (**fig. S7D**), it is plausible that these phagocytes secrete activin to activate ruptoblasts, thereby enhancing the overall clearance of infected cells and pathogens. Collectively, these results

indicate that activin and ruptoblast-mediated responses serve as a secondary host defense complementing phagocytic activity.

Discussion

Our results suggest that in planarians, activin functions both as a hormone and a cytokine, while ruptoblasts act as sentinel cells that specifically respond to activin levels – a mechanism that parallels hormonal surveillance performed by T cells in mammals (*7, 8*). Because both their sensing and killing functions are mediated by diffusive cues, the effective killing range may inherently match the activin-sensing distance, ensuring that cytotoxicity remains spatially restricted to minimize collateral damage. Unlike conventional immune cells, which are activated by pathogens or other immune insults (*42*, *44*), ruptoblasts are triggered solely by activin, highlighting a regulatory mechanism finely attuned to hormonal cues.

As a pro-inflammatory cell type, ruptoblasts may be activated by cells that recognize non-self genotypes and by *cathepsin*$^{+}$ phagocytes that engulf bacteria (*39*), both of which potentially produce activin (**fig. S7E**). It is plausible that ruptoblasts also play regulatory roles by providing feedback to phagocytes for enhanced pathogen clearance, as evidenced by the compromised infection resistance observed upon ruptoblast ablation, while blocking ruptosis alone by *p38-1* RNAi only blocks inflammation (*26*). These observations suggest that ruptoblasts function within a broader immune network, where pro-inflammatory and anti-inflammatory responses must be finely balanced. In addition, analogous to immune exhaustion or other regulatory adaptations of mammalian T cells (*45*), ruptoblasts may develop tolerance to sustained, yet moderate activin levels. Surviving chimeras, for example, had smaller ruptoblasts at lower

densities, indicating a shift toward a less active or immature state. These nuanced regulations invite deeper investigation into the molecular and cellular mechanisms regulating ruptoblast behavior.

Ruptoblasts stand out among cytotoxic immune cells for their explosive mode of action, rivaling the fastest cytotoxic mechanisms reported to date (**Fig. 5G**). While the killing mechanism of invertebrate cytotoxic cells remains largely uncharacterized (*46, 47*), vertebrate cytotoxic cells such as T cells and natural killer (NK) cells rely on direct cell-cell interactions to induce target cell death (*21, 22*). These contact-dependent processes are considerably slower than ruptosis. Although neutrophils can undergo suicidal NETosis, a sacrificial death process that typically unfolds over hours (*48, 49*), their DNA decompacts to form extracellular traps (36, *50*), which does not occur during ruptosis. Instead, entire ruptoblasts, including their nuclei, disintegrate within minutes (**Fig. 3F, 4B**), suggesting that DNA is rapidly cleaved into fragments too small to be detected under light microscopy. Moreover, while neutrophil degranulation and vital NETosis (the release of small extracellular traps without full cell rupture) can occur on a similar timescale as ruptosis (*49*), these processes generally relieve membrane tension and prevent immediate plasma membrane rupture (*50*). This stands in sharp contrast to ruptosis, where rapid membrane rupture occurs immediately. Even in broader comparisons, the hypersensitive response in plants also takes hours for full cellular collapse and pathogen containment (*51*).

These raise intriguing questions about the molecular machinery underlying ruptosis. The sudden vanishing of ruptoblasts suggests an instantaneous massive energy release, potentially driven by a p38-regulated signaling cascade, as p38 knockdown blocks ruptosis. Indeed, the p38 pathway

is known to regulate cytoskeletal rearrangements, facilitating vesicle transport and cortical actin remodeling (*52*) – processes likely essential for ruptosis. Furthermore, the high expression of membrane trafficking and exocytosis genes (e.g., *synaptotagmin*, *stomatin*, *Rab27A*, and *dysferlin* (*53-56*)) in ruptoblasts implies that membrane fusion processes may be critical for ruptosis. Abundantly expressed calcium-binding proteins (e.g., *calretinin*, *calmodulin*, and *calcyphosine*) further supports a calcium-dependent activation step, where endoplasmic reticulum calcium release and extracellular influx may act as triggers for membrane fusion (*57*). However, unlike conventional exocytosis, which stabilizes the plasma membrane, ruptosis culminates in explosive bursting. This suggests that additional mechanisms, such as lipid remodeling, cytoskeleton collapse, or pore formation via novel molecular machinery, should drive the final execution of ruptosis.

Are ruptoblasts unique to planarians? Our sequencing data indicate that they lack canonical immune cell markers, except for *ppib/c*, a cyclophilin-type peptidyl-prolyl cis-trans isomerase known to activate T and B cells in mammals (*58*), and do not express typical cytotoxic killing agents. This suggests that ruptoblasts may derive from a lineage distinct from classical immune cell types and execute cytotoxicity through mechanisms that diverge from known pathways. Strikingly, homologs of *fer3l-1* and another ~30 genes highly expressed in ruptoblasts, including activin receptor, membrane fusion proteins, calcium-binding proteins, and specific cell-type markers such as *ppib/c*, *sspo*, and *galnt* (**Fig. S7F**), are co-expressed in specific cell types across other flatworms (*25*), annelids (*24*), and acoel worms that are sister to all bilaterians (*23*), yet appear absent in cnidarians (e.g., *Hydra* and *Nematostella*) and well-studied models (e.g., vertebrates, flies, and nematodes). This implies that ruptoblasts may represent an ancient,

bilaterian-specific immune cell type that was lost in ecdysozoans and deuterostomes (**Fig. 5H**). They may address the special demand of regenerative animals, concentrated within the Lophotrochozoa superphylum, enabling simultaneous killing of both hormone-secreting cells and stem cells or progenitors that continuously replenish them. Whether ruptoblast-like cells perform similar functions and are regulated by activin in other species remain important open questions.

Altogether, our findings highlight the immense diversity of immune innovations across the animal kingdom and emphasize the need for broader exploration of immune systems beyond conventional models. Elucidating the mechanisms underlying ruptosis will not only uncover unique cell biology processes but also inspire strategies for engineering cytotoxicity or for the disruption of densely packed bacterial biofilms through controlled induction of ruptosis.

References:

1. D. A. Kimbrell, B. Beutler, The evolution and genetics of innate immunity. *Nat. Rev. Genet.* **2**, 256–267 (2001).
2. R. Medzhitov, Recognition of microorganisms and activation of the immune response. *Nature* **449**, 819–826 (2007).
3. M. Schlee, G. Hartmann, Discriminating self from non-self in nucleic acid sensing. *Nat. Rev. Immunol.* **16**, 566–580 (2016).
4. T. Boehm, M. Hirano, S. J. Holland, S. Das, M. Schorpp, M. D. Cooper, Evolution of alternative adaptive immune systems in vertebrates. *Annu. Rev. Immunol.* **36**, 19–42 (2018).
5. M. Hirano, P. Guo, N. McCurley, M. Schorpp, S. Das, T. Boehm, M. D. Cooper, Evolutionary implications of a third lymphocyte lineage in lampreys. *Nature*. **501**, 435-438 (2013).
6. M. F. Flajnik, A cold-blooded view of adaptive immunity. *Nat. Rev. Immunol*. **18**, 438-453 (2018).
7. T. Milo, Y. Korem Kohanim, Y. Toledano, U. Alon, Autoimmune thyroid diseases as a cost of physiological autoimmune surveillance. *Trends Immunol.* **44**, 365–371 (2023).
8. Y. K. Kohanim, A. Tendler, A. Mayo, N. Friedman, U. Alon, Endocrine autoimmune disease as a fragility of immune surveillance against hypersecreting mutants. *Immunity* **52**, 872-884.e5 (2020).
9. A. M. Anderson, L. G. Landry, A. A. Alkanani, L. Pyle, A. C. Powers, M. A. Atkinson, C. E. Mathews, B. O. Roep, A. W. Michels, M. Nakayama, Human islet T cells are highly reactive to preproinsulin in type 1 diabetes. *Proc. Natl. Acad. Sci.* **118**, e2107208118 (2021).
10. A. J. Dwyer, Z. R. Shaheen, B. T. Fife, Antigen-specific T cell responses in autoimmune diabetes. *Front. Immunol.* **15**, 1440045 (2024).
11. S. V. Gearty, F. Dündar, P. Zumbo, G. Espinosa-Carrasco, M. Shakiba, F. J. Sanchez-Rivera, N. D. Socci, P. Trivedi, S. W. Lowe, P. Lauer, N. Mohibullah, A. Viale, T. P. DiLorenzo, D. Betel, A. Schietinger, An autoimmune stem-like CD8 T cell population drives type 1 diabetes. *Nature* **602**, 156–161 (2022).
12. P. W. Reddien, The cellular and molecular basis for planarian regeneration. *Cell* **175**, 327–345 (2018).

13. J. C. Rink, Stem cell systems and regeneration in planaria. *Dev. Genes Evol.* **223**, 67–84 (2013).
14. P. A. Newmark, A. Sánchez Alvarado, Not your father's planarian: a classic model enters the era of functional genomics. *Nat. Rev. Genet.* **3**, 210–219 (2002).
15. J. K. Cloutier, C. L. McMann, I. M. Oderberg, P. W. Reddien, Activin-2 is required for regeneration of polarity on the planarian anterior-posterior axis. *PLOS Genet.* **17**, e1009466 (2021).
16. R. H. Roberts-Galbraith, P. A. Newmark, Follistatin antagonizes Activin signaling and acts with Notum to direct planarian head regeneration. *Proc. Natl. Acad. Sci.* **110**, 1363–1368 (2013).
17. A. G. Tewari, S. R. Stern, I. M. Oderberg, P. W. Reddien, Cellular and molecular responses unique to major injury are dispensable for planarian regeneration. *Cell Rep.* **25**, 2577-2590.e3 (2018).
18. C. P. Arnold, B. W. Benham-Pyle, J. J. Lange, C. J. Wood, A. Sánchez Alvarado, Wnt and TGFβ coordinate growth and patterning to regulate size-dependent behaviour. *Nature* **572**, 655–659 (2019).
19. M. Mihlan, S. Wissmann, A. Gavrilov, L. Kaltenbach, M. Britz, K. Franke, B. Hummel, A. Imle, R. Suzuki, M. Stecher, K. M. Glaser, A. Lorentz, P. Carmeliet, T. Yokomizo, I. Hilgendorf, R. Sawarkar, A. Diz-Muñoz, J. M. Buescher, G. Mittler, M. Maurer, K. Krause, M. Babina, L. Erpenbeck, M. Frank, A. S. Rambold, T. Lämmermann, Neutrophil trapping and nexocytosis, mast cell-mediated processes for inflammatory signal relay. *Cell* **187**, 5316-5335.e28 (2024).
20. M. Faurschou, N. Borregaard, Neutrophil granules and secretory vesicles in inflammation. *Microbes Infect.* **5**, 1317–1327 (2003).
21. D. Keefe, L. Shi, S. Feske, R. Massol, F. Navarro, T. Kirchhausen, J. Lieberman, Perforin triggers a plasma membrane-repair response that facilitates CTL induction of apoptosis. *Immunity* **23**, 249–262 (2005).
22. R. Basu, B. M. Whitlock, J. Husson, A. Le Floc'h, W. Jin, A. Oyler-Yaniv, F. Dotiwala, G. Giannone, C. Hivroz, N. Biais, J. Lieberman, L. C. Kam, M. Huse, Cytotoxic T cells use mechanical force to potentiate target cell killing. *Cell* **165**, 100–110 (2016).
23. R. E. Hulett, J. O. Kimura, D. M. Bolaños, Y.-J. Luo, C. Rivera-López, L. Ricci, M.

Srivastava, Acoel single-cell atlas reveals expression dynamics and heterogeneity of adult pluripotent stem cells. *Nat. Commun.* **14**, 2612 (2023).

24. A. W. Stockinger, L. Adelmann, M. Fahrenberger, C. Ruta, B. D. Özpolat, N. Milivojev, G. Balavoine, F. Raible, Molecular profiles, sources and lineage restrictions of stem cells in an annelid regeneration model. *Nat. Commun.* **15**, 9882 (2024).
25. C. Chai, J. Gibson, P. Li, A. Pampari, A. Patel, A. Kundaje, B. Wang, Flexible use of conserved motif vocabularies constrains genome access in cell type evolution. bioRxiv [Preprint] (2024). https://doi.org/10.1101/2024.09.03.611027.
26. C. P. Arnold, M. S. Merryman, A. Harris-Arnold, S. A. McKinney, C. W. Seidel, S. Loethen, K. N. Proctor, L. Guo, A. Sánchez Alvarado, Pathogenic shifts in endogenous microbiota impede tissue regeneration via distinct activation of TAK1/MKK/p38. *eLife* **5**, e16793 (2016).
27. E. I. Maciel, C. Jiang, P. G. Barghouth, C. J. Nobile, N. J. Oviedo, The planarian *Schmidtea mediterranea* is a new model to study host-pathogen interactions during fungal infections. *Dev. Comp. Immunol.* **93**, 18–27 (2019).
28. H. Thi-Kim Vu, J. C. Rink, S. A. McKinney, M. McClain, N. Lakshmanaperumal, R. Alexander, A. Sánchez Alvarado, Stem cells and fluid flow drive cyst formation in an invertebrate excretory organ. *eLife* **4**, e07405 (2015).
29. H. V. Brøndsted, G. A. Kerkut, *Planarian Regeneration: International Series of Monographs in Pure and Applied Biology: Zoology* (Elsevier Science, Burlington, 1969).
30. O. C. Guedelhoefer, A. Sánchez Alvarado, Planarian immobilization, partial irradiation, and tissue transplantation. *J. Vis. Exp. JoVE*, e4015 (2012).
31. D. E. Wagner, I. E. Wang, P. W. Reddien, Clonogenic neoblasts are pluripotent adult stem cells that underlie planarian regeneration. *Science* **332**, 811–816 (2011).
32. J. T. A. Burrows, D. Depierreux, M. L. Nibert, B. J. Pearson, A Novel taxon of monosegmented double-stranded RNA viruses endemic to Triclad flatworms. *J. Virol.* **94**, e00623-20 (2020).
33. C. Park, K. E. Owusu-Boaitey, G. M. Valdes, P. W. Reddien, Fate specification is spatially intermingled across planarian stem cells. *Nat. Commun.* **14**, 7422 (2023).
34. D. Acharya, R. Reis, M. Volcic, G. Liu, M. K. Wang, B. S. Chia, R. Nchioua, R. Groß, J. Münch, F. Kirchhoff, K. M. J. Sparrer, M. U. Gack, Actin cytoskeleton remodeling primes

RIG-I-like receptor activation. *Cell* **185**, 3588-3602.e21 (2022).

35. J. K. Burkhardt, Cytoskeletal function in the immune system. *Immunol. Rev.* **256**, 5–9 (2013).
36. V. Brinkmann, U. Reichard, C. Goosmann, B. Fauler, Y. Uhlemann, D. S. Weiss, Y. Weinrauch, A. Zychlinsky, Neutrophil extracellular traps kill bacteria. *Science* **303**, 1532–1535 (2004).
37. P. J. Choi, T. J. Mitchison, Imaging burst kinetics and spatial coordination during serial killing by single natural killer cells. *Proc. Natl. Acad. Sci.* **110**, 6488–6493 (2013).
38. C. T. Fincher, O. Wurtzel, T. de Hoog, K. M. Kravarik, P. W. Reddien, Cell type transcriptome atlas for the planarian *Schmidtea mediterranea*. *Science* **360**, eaaq1736 (2018).
39. M. L. Scimone, O. Wurtzel, K. Malecek, C. T. Fincher, I. M. Oderberg, K. M. Kravarik, P. W. Reddien, *foxF-1* controls specification of non-body wall muscle and phagocytic cells in planarians. *Curr. Biol.* **28**, 3787-3801.e6 (2018).
40. M. Evrard, I. W. H. Kwok, S. Z. Chong, K. W. W. Teng, E. Becht, J. Chen, J. L. Sieow, H. L. Penny, G. C. Ching, S. Devi, J. M. Adrover, J. L. Y. Li, K. H. Liong, L. Tan, Z. Poon, S. Foo, J. W. Chua, I.-H. Su, K. Balabanian, F. Bachelerie, S. K. Biswas, A. Larbi, W. Y. K. Hwang, V. Madan, H. P. Koeffler, S. C. Wong, E. W. Newell, A. Hidalgo, F. Ginhoux, L. G. Ng, Developmental analysis of bone marrow neutrophils reveals populations specialized in expansion, trafficking, and effector functions. *Immunity* **48**, 364-379.e8 (2018).
41. V. Papayannopoulos, K. D. Metzler, A. Hakkim, A. Zychlinsky, Neutrophil elastase and myeloperoxidase regulate the formation of neutrophil extracellular traps. *J. Cell Biol.* **191**, 677–691 (2010).
42. M. Walch, F. Dotiwala, S. Mulik, J. Thiery, T. Kirchhausen, C. Clayberger, A. M. Krensky, D. Martinvalet, J. Lieberman, Cytotoxic cells kill intracellular bacteria through granulysin-mediated delivery of granzymes. *Cell* **157**, 1309–1323 (2014).
43. K. Kienle, K. M. Glaser, S. Eickhoff, M. Mihlan, K. Knöpper, E. Reátegui, M. W. Epple, M. Gunzer, R. Baumeister, T. K. Tarrant, R. N. Germain, D. Irimia, W. Kastenmüller, T. Lämmermann, Neutrophils self-limit swarming to contain bacterial growth *in vivo*. *Science* **372**, eabe7729 (2021).
44. T. Kawai, S. Akira, Toll-like receptors and their crosstalk with other innate receptors in

infection and immunity. *Immunity* **34**, 637–650 (2011).

45. C. U. Blank, W. N. Haining, W. Held, P. G. Hogan, A. Kallies, E. Lugli, R. C. Lynn, M. Philip, A. Rao, N. P. Restifo, A. Schietinger, T. N. Schumacher, P. L. Schwartzberg, A. H. Sharpe, D. E. Speiser, E. J. Wherry, B. A. Youngblood, D. Zehn, Defining 'T cell exhaustion.' *Nat. Rev. Immunol.* **19**, 665–674 (2019).
46. B. Rosental, M. Kowarsky, J. Seita, D. M. Corey, K. J. Ishizuka, K. J. Palmeri, S.-Y. Chen, R. Sinha, J. Okamoto, G. Mantalas, L. Manni, T. Raveh, D. N. Clarke, J. M. Tsai, A. M. Newman, N. F. Neff, G. P. Nolan, S. R. Quake, I. L. Weissman, A. Voskoboynik, Complex mammalian-like haematopoietic system found in a colonial chordate. *Nature* **564**, 425–429 (2018).
47. E. A. Mandujano-Tinoco, E. Sultan, A. Ottolenghi, O. Gershoni-Yahalom, B. Rosental, Evolution of cellular immunity effector cells; perspective on cytotoxic and phagocytic cellular lineages. *Cells* **10**, 1853 (2021).
48. H. R. Thiam, S. L. Wong, R. Qiu, M. Kittisopikul, A. Vahabikashi, A. E. Goldman, R. D. Goldman, D. D. Wagner, C. M. Waterman, NETosis proceeds by cytoskeleton and endomembrane disassembly and PAD4-mediated chromatin decondensation and nuclear envelope rupture. *Proc. Natl. Acad. Sci.* **117**, 7326–7337 (2020).
49. S. R. Clark, A. C. Ma, S. A. Tavener, B. McDonald, Z. Goodarzi, M. M. Kelly, K. D. Patel, S. Chakrabarti, E. McAvoy, G. D. Sinclair, E. M. Keys, E. Allen-Vercoe, R. DeVinney, C. J. Doig, F. H. Y. Green, P. Kubes, Platelet TLR4 activates neutrophil extracellular traps to ensnare bacteria in septic blood. *Nat. Med.* **13**, 463–469 (2007).
50. V. Delgado-Rizo, M. A. Martínez-Guzmán, L. Iñiguez-Gutierrez, A. García-Orozco, A. Alvarado-Navarro, M. Fafutis-Morris, Neutrophil extracellular traps and its implications in inflammation: an overview. *Front. Immunol.* **8**, 81 (2017).
51. J.-B. Morel, J. L. Dangl, The hypersensitive response and the induction of cell death in plants. *Cell Death Differ.* **4**, 671–683 (1997).
52. H. Bian, F. Li, W. Wang, Q. Zhao, S. Gao, J. Ma, X. Li, W. Ren, C. Qin, J. Qi, MAPK/p38 regulation of cytoskeleton rearrangement accelerates induction of macrophage activation by TLR4, but not TLR3. *Int. J. Mol. Med.* **40**, 1495–1503 (2017).
53. S. Levy, T. Shoham, The tetraspanin web modulates immune-signalling complexes. *Nat. Rev. Immunol.* **5**, 136–148 (2005).

54. S. D. Catz, The role of Rab27a in the regulation of neutrophil function. *Cell. Microbiol.* **16**, 1301–1310 (2014).
55. R. Han, K. P. Campbell, Dysferlin and muscle membrane repair. *Curr. Opin. Cell Biol.* **19**, 409–416 (2007).
56. Z. Zhu, Z. Guo, X. Gao, Y. Chen, J. Huang, L. Li, B. Sun, Stomatin promotes neutrophil degranulation and vascular leakage in the early stage after severe burn via enhancement of the intracellular binding of neutrophil primary granules to F-actin. *Burns* **50**, 653–665 (2024).
57. M. Trebak, J.-P. Kinet, Calcium signaling in T cells. *Nat. Rev. Immunol.* **19**, 154–169 (2019).
58. S. Gegunde, A. Alfonso, R. Alvariño, E. Alonso, L. M. Botana, Cyclophilins A, B, and C role in human T lymphocytes upon inflammatory conditions. *Front. Immunol.* **12**, 609196 (2021).
59. M. F. Flajnik, M. Kasahara, Origin and evolution of the adaptive immune system: genetic events and selective pressures. *Nat. Rev. Genet.* **11**, 47–59 (2010).
60. Y. Fan, C. Chai, P. Li, X. Zou, J. E. Ferrell, B. Wang, Ultrafast distant wound response is essential for whole-body regeneration. *Cell* **186**, 3606–3618.e16 (2023).
61. T. Stückemann, J. P. Cleland, S. Werner, H. Thi-Kim Vu, R. Bayersdorf, S.-Y. Liu, B. Friedrich, F. Jülicher, J. C. Rink, Antagonistic self-organizing patterning systems control maintenance and regeneration of the anteroposterior axis in planarians. *Dev. Cell* **40**, 248-263.e4 (2017).
62. J. J. Collins, X. Hou, E. V. Romanova, B. G. Lambrus, C. M. Miller, A. Saberi, J. V. Sweedler, P. A. Newmark, Genome-wide analyses reveal a role for peptide hormones in planarian germline development. *PLoS Biol.* **8**, e1000509 (2010).
63. S. R. Bray, L. S. Wyss, C. Chai, M. E. Lozada, B. Wang, Adaptive robustness through incoherent signaling mechanisms in a regenerative brain. *Cell Rep.* **43** (2024).
64. M. A. Grohme, M. Vila-Farré, J. C. Rink, "Small- and Large-Scale High Molecular Weight Genomic DNA Extraction from Planarians" in *Planarian Regeneration: Methods and Protocols*, J. C. Rink, Ed. (Springer, New York, NY, 2018; https://doi.org/10.1007/978-1-4939-7802-1_7), pp. 267–275 (2018).
65. R. S. King, P. A. Newmark, In situ hybridization protocol for enhanced detection of gene

expression in the planarian Schmidtea mediterranea. *BMC Dev. Biol.* **13**, 8 (2013).

66. B. Stubenhaus, J. Pellettieri, Detection of apoptotic cells in planarians by whole-mount TUNEL. *Methods Mol. Biol. Clifton NJ* **1774**, 435–444 (2018).
67. A. Rozanski, H. Moon, H. Brandl, J. M. Martín-Durán, M. A. Grohme, K. Hüttner, K. Bartscherer, I. Henry, J. C. Rink, PlanMine 3.0—improvements to a mineable resource of flatworm biology and biodiversity. *Nucleic Acids Res.* **47**, D812–D820 (2019).
68. B. Langmead, S. L. Salzberg, Fast gapped-read alignment with Bowtie 2. *Nat. Methods* **9**, 357–359 (2012).
69. M. I. Love, W. Huber, S. Anders, Moderated estimation of fold change and dispersion for RNA-seq data with DESeq2. *Genome Biol.* **15**, 550 (2014).
70. Y. Thappeta, S. J. Cañas-Duarte, T. Kallem, A. Fragasso, Y. Xiang, W. Gray, C. Lee, L. Cegelski, C. Jacobs-Wagner, Glycogen phase separation drives macromolecular rearrangement and asymmetric division in *E. coli*. bioRxiv [Preprint] (2024). https://doi.org/10.1101/2024.04.19.590186
71. T. Smith, A. Heger, I. Sudbery, UMI-tools: modeling sequencing errors in Unique Molecular Identifiers to improve quantification accuracy. *Genome Res.* **27**, 491–499 (2017).
72. M. Martin, Cutadapt removes adapter sequences from high-throughput sequencing reads. *EMBnet.journal* **17**, 10–12 (2011).
73. M. D. Young, S. Behjati, SoupX removes ambient RNA contamination from droplet-based single-cell RNA sequencing data. *GigaScience* **9**, giaa151 (2020).
74. I. Korsunsky, N. Millard, J. Fan, K. Slowikowski, F. Zhang, K. Wei, Y. Baglaenko, M. Brenner, P. Loh, S. Raychaudhuri, Fast, sensitive and accurate integration of single-cell data with Harmony. *Nat. Methods* **16**, 1289–1296 (2019).
75. A. J. Tarashansky, Y. Xue, P. Li, S. R. Quake, B. Wang, Self-assembling manifolds in single-cell RNA sequencing data. *eLife* **8**, e48994 (2019).
76. D. M. Emms, S. Kelly, OrthoFinder: phylogenetic orthology inference for comparative genomics. *Genome Biol.* **20**, 238 (2019).
77. J. Huerta-Cepas, D. Szklarczyk, D. Heller, A. Hernández-Plaza, S. K. Forslund, H. Cook, D. R. Mende, I. Letunic, T. Rattei, L. J. Jensen, C. von Mering, P. Bork, eggNOG 5.0: a hierarchical, functionally and phylogenetically annotated orthology resource based on 5090 organisms and 2502 viruses. *Nucleic Acids Res.* **47**, D309–D314 (2019).

78. A. Regev, S. A. Teichmann, E. S. Lander, I. Amit, C. Benoist, E. Birney, B. Bodenmiller, P. Campbell, P. Carninci, M. Clatworthy, H. Clevers, B. Deplancke, I. Dunham, J. Eberwine, R. Eils, W. Enard, A. Farmer, L. Fugger, B. Göttgens, N. Hacohen, M. Haniffa, M. Hemberg, S. Kim, P. Klenerman, A. Kriegstein, E. Lein, S. Linnarsson, E. Lundberg, J. Lundeberg, P. Majumder, J. C. Marioni, M. Merad, M. Mhlanga, M. Nawijn, M. Netea, G. Nolan, D. Pe'er, A. Phillipakis, C. P. Ponting, S. Quake, W. Reik, O. Rozenblatt-Rosen, J. Sanes, R. Satija, T. N. Schumacher, A. Shalek, E. Shapiro, P. Sharma, J. W. Shin, O. Stegle, M. Stratton, M. J. T. Stubbington, F. J. Theis, M. Uhlen, A. van Oudenaarden, A. Wagner, F. Watt, J. Weissman, B. Wold, R. Xavier, N. Yosef, The Human Cell Atlas. *eLife* **6**, e27041 (2017).
79. H. Li, J. Janssens, M. De Waegeneer, S. S. Kolluru, K. Davie, V. Gardeux, W. Saelens, F. P. A. David, M. Brbić, K. Spanier, J. Leskovec, C. N. McLaughlin, Q. Xie, R. C. Jones, K. Brueckner, J. Shim, S. G. Tattikota, F. Schnorrer, K. Rust, T. G. Nystul, Z. Carvalho-Santos, C. Ribeiro, S. Pal, S. Mahadevaraju, T. M. Przytycka, A. M. Allen, S. F. Goodwin, C. W. Berry, M. T. Fuller, H. White-Cooper, E. L. Matunis, S. DiNardo, A. Galenza, L. E. O'Brien, J. A. T. Dow, FCA Consortium, H. Jasper, B. Oliver, N. Perrimon, B. Deplancke, S. R. Quake, L. Luo, S. Aerts, Fly Cell Atlas: A single-nucleus transcriptomic atlas of the adult fruit fly. *Science* **375**, eabk2432 (2022).
80. M. Lange, A. Granados, S. VijayKumar, J. Bragantini, S. Ancheta, Y.-J. Kim, S. Santhosh, M. Borja, H. Kobayashi, E. McGeever, A. C. Solak, B. Yang, X. Zhao, Y. Liu, A. M. Detweiler, S. Paul, I. Theodoro, H. Mekonen, C. Charlton, T. Lao, R. Banks, S. Xiao, A. Jacobo, K. Balla, K. Awayan, S. D'Souza, R. Haase, A. Dizeux, O. Pourquie, R. Gómez-Sjöberg, G. Huber, M. Serra, N. Neff, A. O. Pisco, L. A. Royer, A multimodal zebrafish developmental atlas reveals the state-transition dynamics of late-vertebrate pluripotent axial progenitors. *Cell* **187**, 6742-6759.e17 (2024).
81. Y. K. Dhuriya, D. Sharma, Necroptosis: a regulated inflammatory mode of cell death. *J Neuroinflammation* **15**, 199 (2018).
82. D. Bertheloot, E. Latz, B. S. Franklin, Necroptosis, pyroptosis and apoptosis: an intricate game of cell death. *Cell. Mol. Immunol.* **18**, 1106-1121 (2021).
83. J. Yuan, D, Ofengeim, A guide to cell death pathways, *Nat. Rev. Mol. Cell Biol.* **25**, 379-395 (2024).

84. J. Li, F. Cao, H. Yin, Z. Huang, Z. Lin, N. Mao, B. Sun, G. Wang, Ferroptosis: past, present and future. *Cell Death Dis.* **11**, 88 (2020).
85. Y. Wang, N. Kim, J. Haince, H. Kang, K. David, S. Andrabi, G. Poirier, V. Dawson, T. Dawson, Poly(ADP-Ribose)(PAR) binding to apoptosis-inducing factor is critical for PAR polymerase-1-dependent cell death (Parthanatos). *Sci. Signal* **4**, ra20-ra20 (2011).
86. J. Kim, L. He, J. J Lemasters, Mitochondrial permeability transition: a common pathway to necrosis and apoptosis, *Biochem. Biophys. Res. Commun*. **304**, 463-470 (2003).

Acknowledgements

We thank Hanh Vu and Jochen Rink for sharing the ef1α antibody and stimulating discussions, Christopher Arnold for sharing the *Pseudomonas* bacteria, Uri Alon and Hawa Racine Thiam for critical discussions, Jesse Gibson, Livia Wyss, Margarita Khariton, Christopher He, and Kelli Ann Lynch for experimental help and all Wang group members for feedback. C.C. is supported by a Stanford DARE fellowship. This work is supported by an NIH grant (1R35GM138061) to B.W. and a HFSP grant (RGY0085/2019) to B.W. and B.R.

Author contributions

CC, BR, and BW designed the research. CC, ES, and LZ performed *ex vivo* experiments. CC performed sequencing experiments and analyzed the data. CC, SRS, and DNS performed functional experiments. OY helped recombinant ACT-2 protein production. CJW provided advice on bacterial cell killing assay. CC and BW wrote the paper with input from all other authors. BR and BW acquired funding and supervised the project.

Competing interests: The authors declare no competing interests.

Data and Material Availability:

Raw and processed bulk RNA and scRNA-seq datasets generated in this study are available from NCBI BioProject with accession number PRJNA1233892 (bulk RNAseq) and PRJNA1233887 (scRNAseq). Any additional data or material required to reproduce or re-analyze will be made available from the lead authors upon request.

Supporting Materials

Materials and Methods

Figs. S1 to S7

Tables S1 to S3

References (60-86)

Movies S1 to S5

Figures

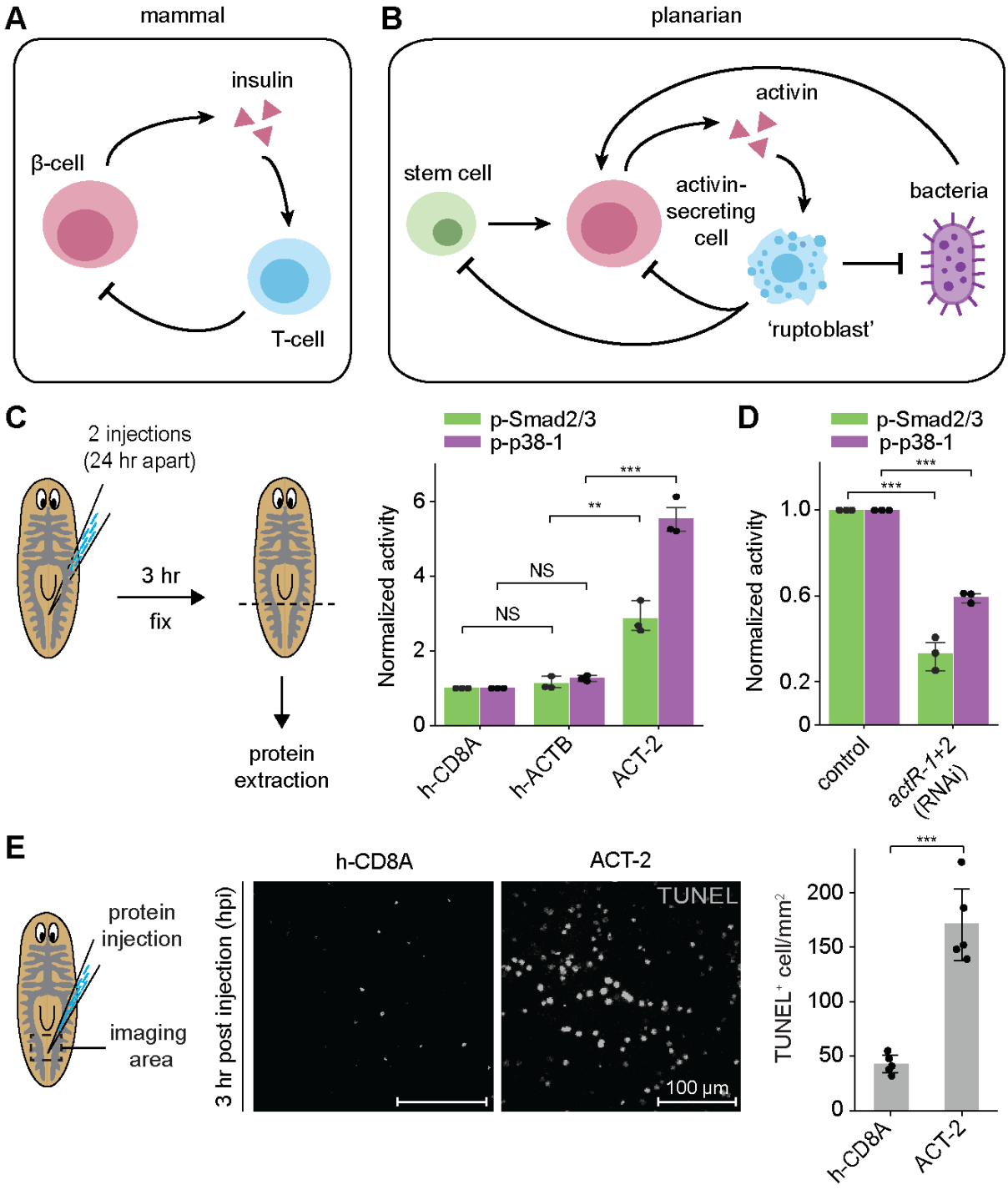

Fig. 1. ACT-2 induces inflammatory responses in planarians.

(A) Schematics showing T-cell-mediated elimination of hormone-hypersecreting cells in mammals, using insulin-producing β-cells as an example.

(B) Proposed activin surveillance mechanism in planarians in which overactivation of activin signaling causes 'ruptoblasts' to eliminate stem cells, activin-secreting cells, and microbes.

(C) Quantification of p-Smad2/3 (green) and p-p38-1 (magenta) levels using Western blotting in control animals (injected with h-CD8A, h-ACTB) and animals injected with ACT-2 into the parenchymal tissue between posterior gut branches. Tail tissues (posterior to the dashed line) were collected for protein extraction.

(D) ACT-2 injection-induced increase of p-Smad2/3 and p-p38-1 is reduced by RNAi-mediated knockdown of *actR1* and *actR2*.

(E) (Left) Representative image of TUNEL staining at the injection site showing cell death at 3 hours post injection (hpi) in animals injected with h-CD8A and ACT-2 proteins, respectively. Dashed boxes: imaging area. (Right) Number of TUNEL$^+$ cells near the injection site.

Data points in (C-D) represent biological replicates each containing tail tissue fragments from five animals, and in (E) individual animals pooled from two independent experiments. Statistical significance is determined by a two-sided t-test, with error bars denoting standard deviation (SD). **$p < 0.01$, ***$p < 0.001$, NS, not significant.

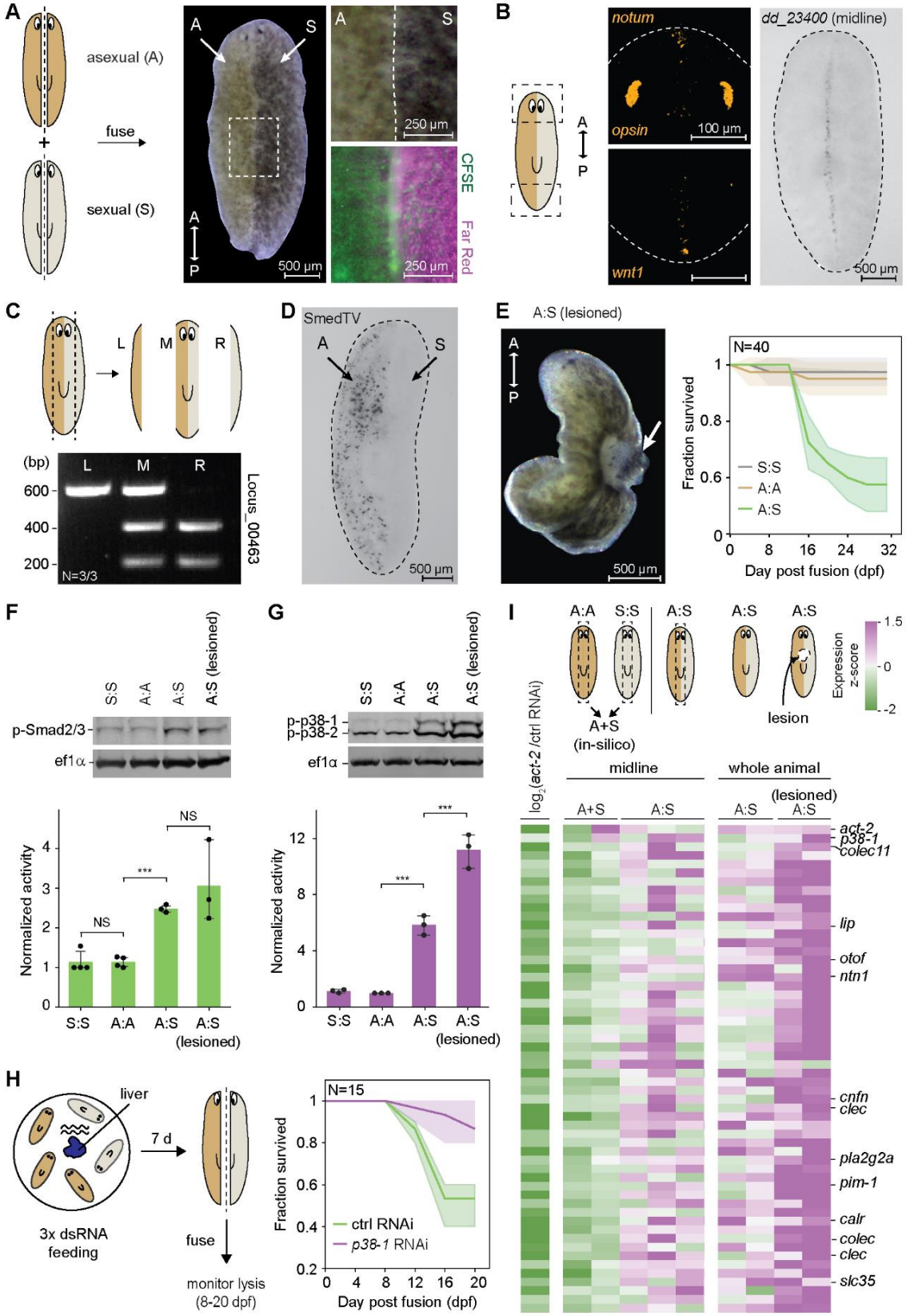

Fig. 2. Genetic chimerism induces activin overactivation, resulting in chronic inflammation.

(A) Planarians of two distinct genotypes, asexual (A) and sexual (S), are cut longitudinally along the midline and fused to form a chimera. Note the different pigmentation of tissues from two genotypes. Right: a magnified view showing the fusion site in bright field (top), in fluorescence (bottom) using pre-stained CellTrace CFSE and Far Red at 3 days post fusion (dpf).

(B) (Left) FISH images showing expression of *notum* in the anterior pole and *wnt-1* in the posterior pole of genetic chimeras at 20 dpf. (Right) WISH image showing a single midline marked by *dd_23400* in genetic chimeras at 20 dpf.

(C) PCR-RFLP analysis of tissues collected from the left (L), middle (M), and right (R) portions of the chimera body. Genotyping is based on locus 00463 cut by ScaI in sexual cells but not in asexual cells.

(D) WISH image showing the expression of asexual-specific RNA virus SmedTV in genetic chimeras at 20 dpf. Note the clear division between asexual and sexual halves.

(E) (Left) Brightfield image of a chimera with a lesion at the fusion site. (Right) Survival curves of chimeras and homotypic fusions.

(F-G) (Top) Western blot showing p-Smad2/3 (F) and p-p38-1(G) in chimeras with lesions at 14–18 dpf and without lesions at 20 dpf, compared to homotypic fusions. (Bottom) Quantified fold activation normalized to the levels in sexual homotypic fusions.

(H) (Left) Schematics showing the workflow of RNAi feeding before fusion. (Right) *p38-1* RNAi reduced the fraction of lesioned chimeras. Since *act-2* RNAi induces anteroposterior (AP) axis bifurcation (*15*), preventing chimeric fusion. Consequently, this precludes a direct test of whether *act-2* RNAi can mitigate lesion.

(I) (Left) Heatmap showing expression fold change after *act-2* RNAi (*15*). (Middle) Normalized expression comparing midlines of chimeras without lesions to that of numerical average of

sexual and asexual homotypic fusions. Genes significantly upregulated (p-value < 0.05, two-sided Welch's t-test) were shown with *act-2* and *p38-1* added to the top. Genes labeled have immune functions in other organisms. (Right) Comparison of lesioned and non-lesioned chimeras show that the upregulation in chimeras are further amplified during lesion.

N in (C) denotes the number of biological replicates that show results consistent with the gel image. SD of survival curves in (E, H) was obtained from three independent experiments with N denoting the total number of animals monitored. Data points in (F, G) represent biological replicates each containing three chimeras. Statistical significance is determined by a two-sided t-test, with error bars denoting SD. ***p <0.001, NS, not significant.

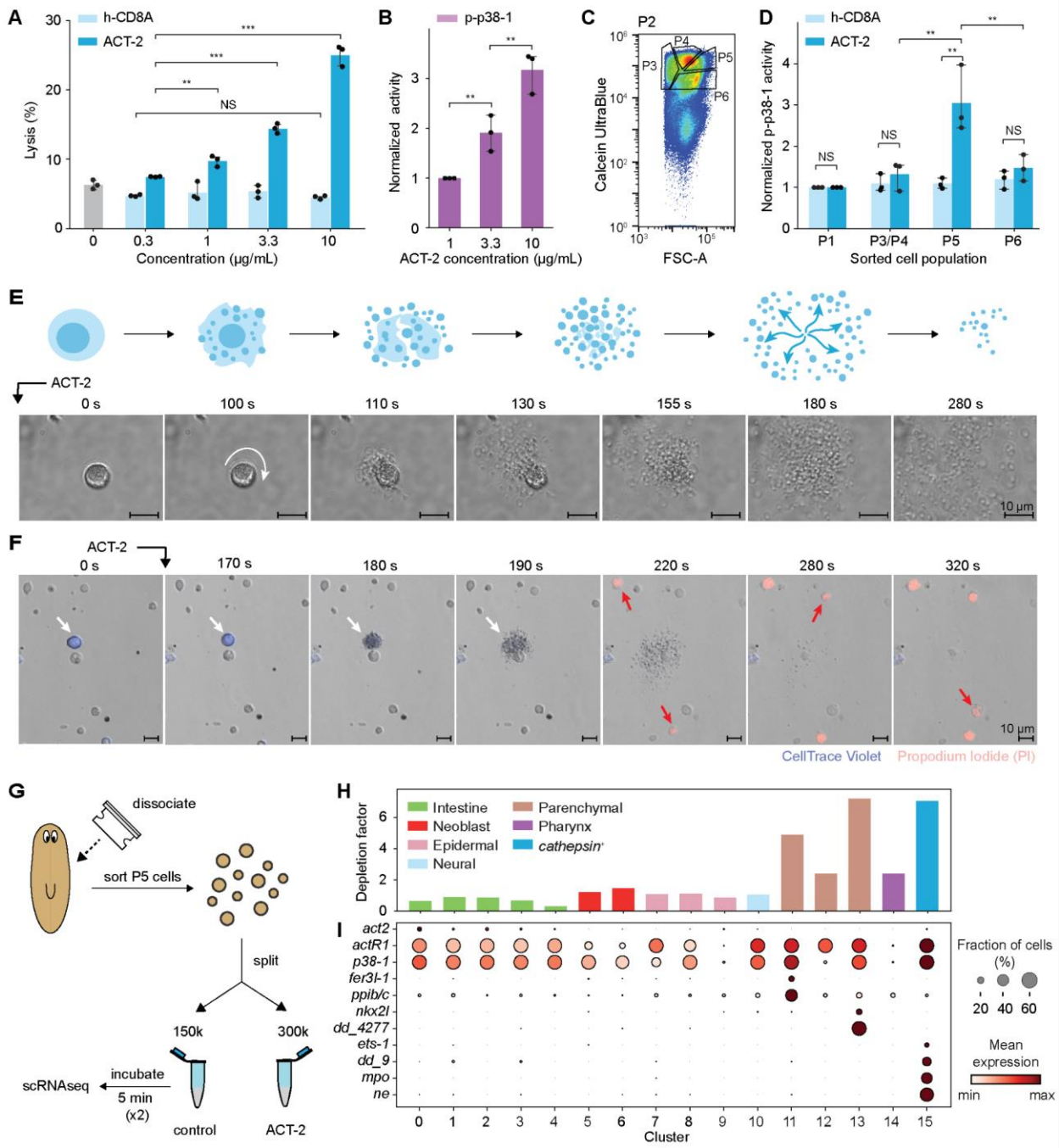

Fig. 3. Ruptoblasts and their molecular identity.

(A) Cell lysis measured via flow cytometry in response to varying concentrations of h-CD8A (control) and ACT-2 proteins, quantified by the percentage of PI^+ cells.

(B) Quantification of p-p38-1 in bulk cells following exposure to increasing concentrations of ACT-2.

(C) Sorting strategy for enriching activin-responding cells based on Calcein Ultrablue stain and forward scattering (FSC), after an initial back scatter (BSC, measuring granularity) gating shown in **fig. S5A**.

(D) Barplot quantifying p-p38-1 in sorted subpopulations following exposure to 10 μg/mL h-CD8A or ACT-2. P1 is a low back scattering control population (**fig. S5A**). P3 and P4 were pooled for Western blot to collect sufficient material.

(E) Schematics (top) and snapshot images (bottom) of ruptosis. Note the initial spin of the cell (white arrow) followed by degranulation and membrane rupture between 100-110 s after adding ACT-2, and the complete dissolution of the cell, including the nucleus, between 130-155 s post treatment. The corresponding video is shown in **movie S3**.

(F) Snapshots demonstrating that sorted P5 cells (CellTrace Violet-labeled) can kill nearby unlabeled cells (pooling P1, P3, P4, P6). Cell death is indicated by PI entry (red). Cells were mixed at a 1:4 ratio of P5 to the rest. ACT-2 was added at ~90 s. White arrow: ruptoblast, red arrows: killed cells. The corresponding video is shown in **movie S4.**

(G) Schematics showing the strategy to identify the molecular identity of ruptoblasts. Note the cells were incubated with h-CD8A or ACT-2 twice for 5 min each before proceeding with sequencing (see Methods).

(H) Depletion factor for each cell cluster, defined as the ratio of cell abundance between h-CD8A and ACT-2 treated samples.

(I) Dotplot showing expression of *act2*, *actR1*, and *p38-1* along with select cluster markers and immune related-genes in each cell cluster. Color: mean expression calculated across control and ACT-2 treated conditions, dot size: fraction of expressing cells. The broad expression patterns of *actR1* and *p38-1* were also consistently observed in the planarian cell atlas (*38*).

Data points represent biological replicates each consisting of 50,000 cells in (A), and 300,000 cells in (B, D). Statistical significance is determined by a two-sided t-test, with error bars denoting SD from three independent experiments. **$p < 0.01$, ***$p < 0.001$, NS, not significant.

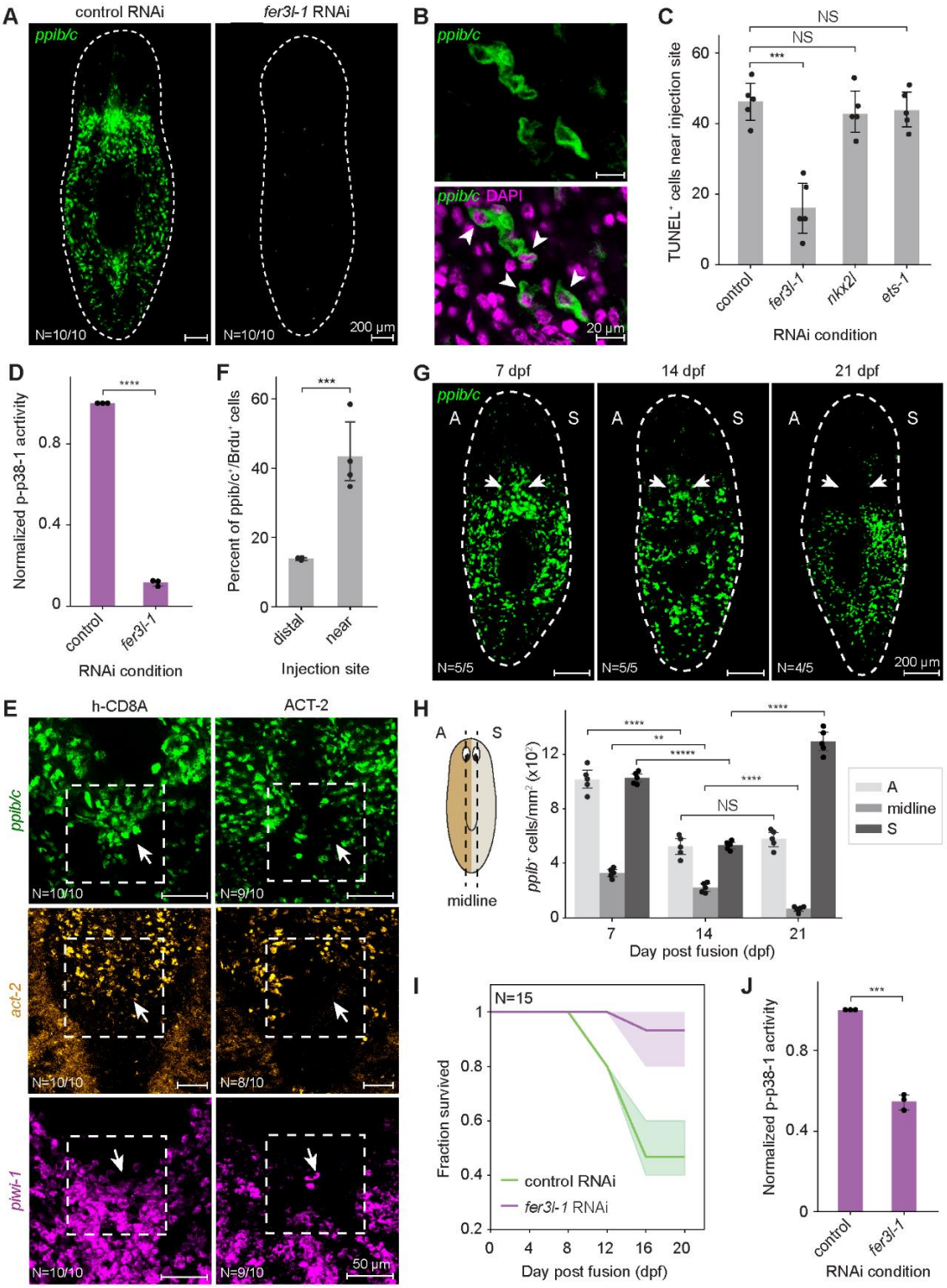

Fig. 4. Ruptoblast-mediated cytotoxicity *in vivo*.

(A) FISH showing the expression of *ppib/c* (*dd_348*) in control and *fer3l-1* (*dd_8096*) RNAi planarians. Dashed lines: animal outline.

(B) Higher magnification image showing *ppib/c* in green (top) along with DAPI staining in magenta (bottom) demonstrating the presence of intact nuclei in ruptoblasts (arrows).

(C) TUNEL$^+$ cells counted near the injection site for control, *fer3l-1, nkx2l (dd_13898),* and *ets-1 (dd_2092)* RNAi-treated animals 3 hr post ACT-2 injections.

(D) ACT-2-induced p38-1 activation is reduced in *fer3l-1* RNAi animals at 3 hpi, with p-p38-1 levels normalized against the control.

(E) ACT-2 injection ablate ruptoblasts (top), activin-secreting cells (middle) and neoblasts (bottom) at the injection site (dashed boxes and arrows).

(F) Quantification of newly differentiated ruptoblasts (BrdU$^+$/*ppib/c*$^+$) in regions distant from and near the injection site at 5 d post-ACT-2 injection.

(G) FISH showing the distribution of ruptoblasts in chimeras at 7, 14 and 21 dpf. A: asexual side, S: sexual side, dashed lines: animal outline. White arrows highlight the decrease in ruptoblast density along the midline.

(H) Density of ruptoblasts in asexual (A) side, midline region where asexual and sexual cells interact, and sexual (S) side in chimeras at 7, 14, and 21 dpf.

(I-J) *fer3l-1* RNAi reduces lesioned fraction (I) and p-p38-1 levels (J) in chimeras.

N in (A, E, G) represents the number of animals showing the phenotype among all examined. Data points in (C, F, H) represent individual animals pooled from two independent experiments, in (D, J) represent biological replicates, with each containing three animals. SD of the survival curves in (I) is from three independent experiments with N denoting the total number of animals monitored. Statistical significance was determined by a two-sided t-test, with SD as error bars. **$p < 0.01$, ***$p < 0.001$, ****$p < 0.000l$, NS, not significant.

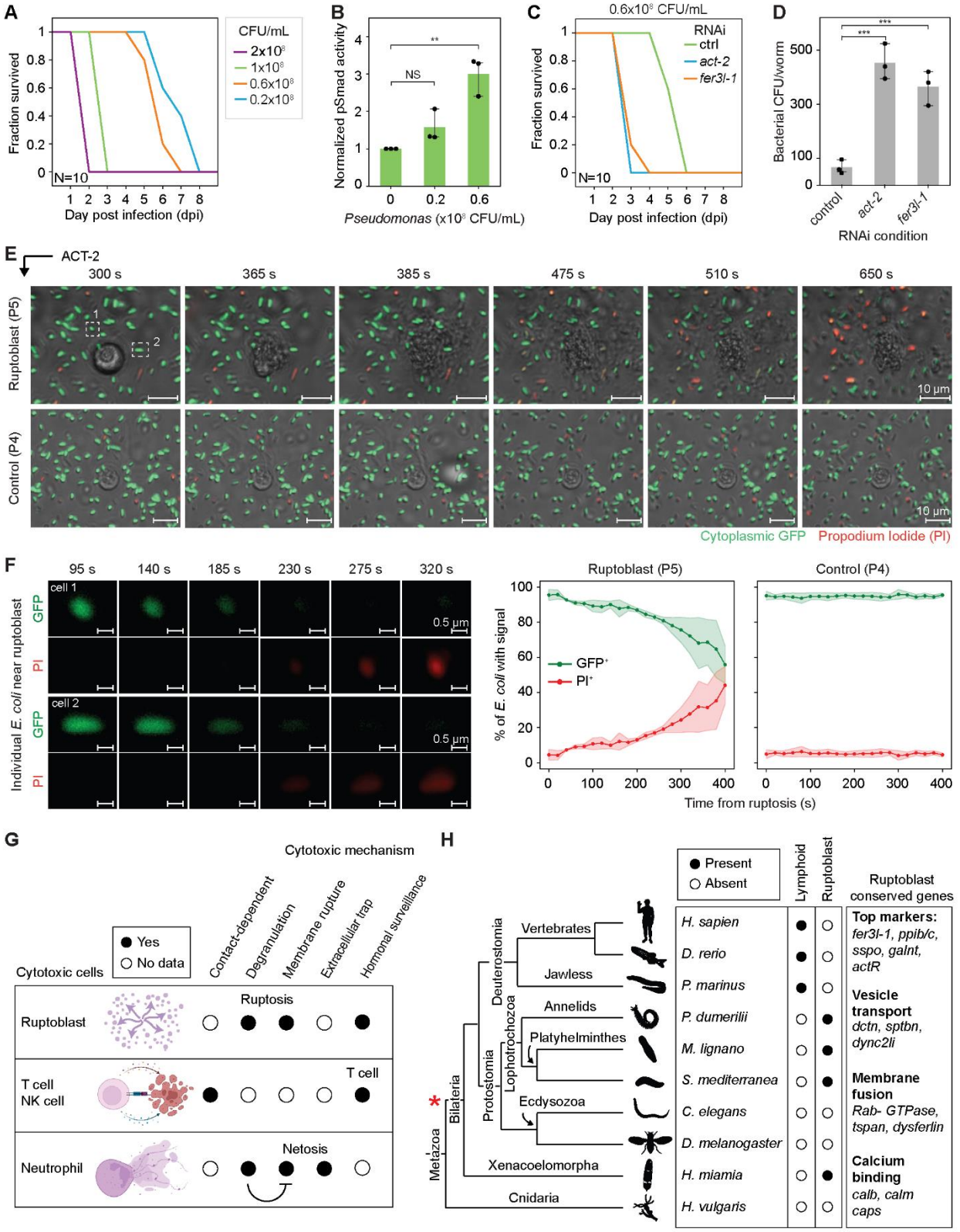

Fig. 5. Broad immune functions of ruptoblasts.

(A) Survival curves of asexual planarians exposed to varying concentrations of pathogenic *Pseudomonas*.

(B) p-Smad2/3 level in animals exposed to different *Pseudomonas* concentrations.

(C) Survival curves of *act-2* and *fer3l-1* RNAi animals exposed to $0.6x10^8$ CFU/mL of *Pseudomonas*.

(D) Quantification of commensal bacterial load in control, *act-2* and *fer3l-1* RNAi animals.

(E) Representative snapshots showing that ruptoblasts kill nearby *E. coli* (top) upon adding ACT-2 whereas non-ruptoblast P4 cells (bottom) do not. *E. coli* death is evidenced by the loss of cytoplasmic GFP (green) followed by PI uptake (red). White dashed boxes highlight the two *E. coli* cells shown in F. The corresponding video is shown in **movie S5**.

(F) (Left) Magnified snapshots of individual *E. coli* undergoing cell death following ruptosis. The loss of cytoplasmic GFP signal occurs abruptly within 45 s, followed by PI uptake in the next 1.5 min, indicating that both inner and outer membranes are permeabilized by the killing agents released by ruptoblasts. (Right) Quantification of the fractions of GFP^+ and PI^+ *E. coli* over time, illustrating the kinetics of bacterial death at the population level. SD is calculated from three experiments, with time zero set at the onset of ruptosis.

(G) Summary of diverse cytotoxic strategies utilized by immune cells. Ruptoblasts kill through a mechanism distinct from how T cells, NK cells, and neutrophils kill. While neutrophils can also degranulate, unlike ruptoblasts, neutrophil degranulation inhibits membrane rupture as indicated by the inhibition arrow. Notably, among the cytotoxic cells, only ruptoblasts and T cells are capable of responding to hormonal activation.

(H) Ruptoblast is likely an ancient cytotoxic cell type, whereas lymphoid cytotoxic cells are vertebrate specific (*4, 46, 59*). Filled circles: presence, empty circles: absence, based on gene

expression. Red star: proposed evolutionary origin of ruptoblasts. Genes conserved in all identified ruptoblast-like cells are listed on the right.

N in (A, C) represents the total number of animals monitored. Data points in (B, D) represent biological replicates, each containing three animals. Statistical significance is determined by a two-sided t-test, with SD indicated by error bars. $^{**}p < 0.01$, $^{***}p < 0.001$, NS, not significant.

Materials and Methods

Animal maintenance:

Asexual (CIW4) and sexual (S2F2) *S. mediterranea* were maintained in the dark at 18 °C in 0.5 g/L Instant Ocean Sea Salts (IO) supplemented with 0.1 g/L sodium bicarbonate (asexual planarian media) and 0.75× Montjuic salts (sexual planarian media), respectively. Planarians were fed calf liver paste weekly, and starved for 7 days prior to all experiments.

ACT-2 recombinant protein:

Between human activin (h-ACTB) and the planarian ACT-2, sequence conservation is restricted to the TGF-β domain, with no homology detected elsewhere, and only 29% amino acid identity within the domain. Given this low similarity, h-ACTB is unlikely to functionally substitute for ACT-2. Therefore, we produced ACT-2 recombinant protein using a yeast expression system (Cusabio, Cat#CSB-EP3606GOQ1) to ensure proper glycosylation of the secreted protein. A 6× His-tag was added to the N-terminus. The protein was assessed by SDS-PAGE to have 88% purity. Endotoxin level, measured using the Limulus amebocyte lysate (LAL) assay, was below 1.0 endotoxin unit (EU) per microgram of protein.

Protein injection:

20 μg/mL of control proteins – h-CD8A (Cusabio, Cat#YP004966HU) or h-ACTB (SinoBiological, Cat#10429-HNAH) – or ACT-2 protein (20 μg/mL) was loaded into needles pulled from glass capillaries (WPI, Cat#1B00F-3) on a Sutter P97 needle puller with the following settings: pressure = 500, heat = 758, pull = 50, velocity = 70, time = 200. Needles were mounted on a Sutter XenoWorks injection system, and tips were carefully opened with

forceps. Animals were positioned ventral-side up on a moist filter paper placed on a cooled block and injected along the tail midline until a visible bolus formed and ceased expanding. Following injection, animals were allowed to recover in the dark at 18 °C before downstream processing.

Western blotting:

Animals were fixed in 100 mM $ZnCl_2$ fixative for 1 hr at 4 ºC (*60, 61*). Lysate was obtained by homogenizing ~3-5 animals in urea-based lysis buffer (9 M urea, 2% SDS, 130 mM DTT, 10× protease inhibitor cocktail, 1× phosphatase, benzonase) using an electronic pestle homogenizer, and incubated for 30 min, and spun down at ~ 22,000 × g at room temperature (RT) for 10 min. Protein concentrations were determined by absorbance at 280 nm on a Nanodrop.

Samples were mixed with 1× LDS buffer and denatured at 70 ºC. SDS-PAGE was performed using NuPAGE Novex 4-12 % gels, and proteins were transferred to nitrocellulose membranes via either wet transfer blot module (Invitrogen) or iBlot2 dry transfer (Invitrogen). The blot was blocked in Intercept blocking buffer (LI-COR), then incubated overnight with primary antibody (1:1,000 anti-p-Smad2, Cell Signaling Technology; 1:100,000 anti-ef1α, a gift from Jochen Rink's lab generated at MPI-CBG; 1:1000 anti-p-p38, Cell Signaling Technology) in Intercept T20 (TBS) antibody diluent solution (LICORbio, Cat# 927-65001). After washing, membranes were incubated with secondary antibodies (1:20,000 anti-rabbit IRDye 800CW, LI-COR; 1:10,000 anti-mouse-Igg1-555, Biotium) in Intercept T20 (PBS) antibody diluent solution (LICORbio, Cat# 927-75001) for 1 hr. Final washes were in PBS supplemented with 0.1% Tween-20 followed by PBS alone.

Blots were imaged with a LI-COR Odyssey imager at 800 and 680 nm, and Typhoon 9500 at 555 nm. Images were quantified using ImageJ gel plugins. p-Smad2/3 and p-p38-1 levels were normalized across samples to ef1α, and fold activation of pSmad2/3 and p-p38-1 were determined by normalizing to their respective control conditions.

For performing Western blotting on cells, the same procedure was followed, except that cells were directly lysed in the urea-based lysis buffer. A 1:50,000 dilution of anti-ef1α and 1:5,000 dilution of anti-mouse-Igg1-555 were used.

Planarian fusion:

Sexual and asexual planarians (~3 mm in length) were fed double stranded RNA (dsRNA) against *pc2* every 4 d for 3 feedings to immobilize animals (*62, 63*) required for the fusion procedure. With this body size, sexual planarians do not develop gonads. Starved animals were cut longitudinally along the midline on an iced Coolrack with weigh paper. To fluorescently label tissues, animals were soaked overnight in CellTrace CFSE (1:1,000, Invitrogen, Cat# C34554) or Celltrace Far Red (1:1,000, Invitrogen, Cat# C34564). Opposite halves of the asexual and sexual worms were pushed together and covered with Zig-Zag cigarette rolling paper, and constrained by four pieces of filter paper and a Kimwipe soaked with asexual planarian media on the side (**fig. S3A**). Fusions were left overnight at 10 ^{o}C and transferred to 1:1 mixture of Montjuic and IO salts with 1:1,000 gentamicin.

Genotyping:

Genomic DNA was extracted as previously described (*64*). Restriction Fragment Length Polymorphism (RFLP-00463) loci (*31*) were amplified from genomic DNA using Phusion Polymerase using 35-40 PCR cycles. PCR products were purified, digested with ScaI-HF restriction enzyme for 2 hr, and ran on a 1% agarose gel.

Staining:

Riboprobes for in situ hybridization were synthesized as previously described (*62*). Gene fragments were amplified from cDNA using oligonucleotide primers listed in **table S2**, and cloned into pJC53.2 (Addgene Plasmid ID: 26536).

RNA WISH and FISH were performed as described (*65*). Briefly, planarians were relaxed on ice, killed in 5% N-Acetyl Cysteine (NAC) for 5 min, then fixed for 2 hr in 4% formaldehyde supplemented with 1% NP-40 at RT. After dehydration in methanol (stored at -20 ^{o}C if needed), planarians were rehydrated and bleached for 2 hr in the bleaching solution (5% formamide, 0.5× SSC, 1.2% H_2O_2) under bright light. They were permeabilized with 2 μg/mL proteinase K for 10 min, and post-fixed with 4% formaldehyde. Hybridization was performed at 56 ^{o}C overnight. Detection used either NBT/BCIP for WISH or tyramide signal amplification for FISH.

For immunostaining, planarians were relaxed on ice, killed in 2% HCl for 5 min, fixed for 6 hr at 4 ^{o}C in 4% formaldehyde, and bleached overnight in 6% H_2O_2. Samples were blocked in 1% (w/v) BSA in PBSTx for 4 hr, incubated overnight with primary antibodies (1:1,000 6G10, DSHB; 1:1,000 anti-SYNORF1, 3C11, DSHB), followed by 1 hr blocking. Secondary antibodies

(1:1,000 goat-anti-mouse IgG+IgM conjugated with peroxidase) were added overnight, and detected by tyramide signal amplification.

For TUNEL staining (*66*), planarians were relaxed on ice, killed in 5% NAC for 10 min, fixed in 4% formaldehyde for 20 min at RT, and bleached in 6% H_2O_2 overnight under bright light. They were then incubated in TdT enzyme mix for 4 hr at 37 ^{o}C, followed by stop/wash buffer for 10 min, and rhodamine-labeled antibody for 4 hr at RT. TdT enzyme mix, stop/wash buffer, and rhodamine antibody were obtained from Millipore ApopTag Red Kit (Cat# S7165).

BrdU labeling with RNA-FISH used a protocol described in (*28*). Briefly, 2 μL of BrdU stock (20 mg/mL in 50% DMSO, Roche, Cat# 10280879001) was mixed with 8 μL of beef extract and fed to asexual planarians. During the BrdU chase, animals were maintained in 5× IO salts. They were then killed in 5% NAC, fixed in 4% formaldehyde for 30 min at RT, bleached in 6% H_2O_2 in methanol. After standard RNA FISH, samples were treated with 2N HCl containing 0.3% Triton X-100 for 30 min at RT, washed in PBSTx, and blocked in 5% RWBR and 5% horse serum for 2 hr at RT. Samples were incubated with anti-BrdU (Abcam ab6326, 1:1,000) in 4 ^{o}C overnight, washed, and then incubated overnight at 4 ^{o}C with anti-rat HRP (Cell Signaling Technology, Cat#7077, 1:1,000). Detection used tyramide signal amplification.

Microscopy and image analysis:

WISH samples were mounted in 80% glycerol supplemented with 10 mM Tris and 1 mM EDTA, pH = 7.5. Bright-field and WISH images were captured using a Canon EOS M50 mounted on a Zeiss Stemi 508 microscope. Samples for fluorescence imaging were mounted in scale solution

(30% glycerol, 0.1% Triton X-100, 2 mg/mL sodium ascorbate, 4 M urea in PBS) and imaged on a Zeiss LSM 800 confocal microscope using 20× water immersion objective (N.A. = 1.0, working distance = 1.8 mm). All fluorescence images shown are maximum intensity projections and are representative of images taken in each condition. Cell counts (e.g., TUNEL$^+$ or *ppib/c*$^+$ cells) were quantified using the Fiji multi-point tool to mark cells through confocal z-stacks.

RNAi:

dsRNA was prepared by *in vitro* transcription as described previously (*62*). For RNAi through feeding, dsRNA was mixed with liver paste at a concentration of ~150 ng/µL and fed to planarians every 4 d for 8 feedings for activin and activin receptor knockdowns, 3 feedings for *p38-1*, and 6 feedings for *fer3l-1, nkx2l, and ets-1*. For *act-2* RNAi in sexual planarians, animals were fed every 4 days for a total of 6 feedings. In all experiments, dsRNA matching ccdB and camR-containing insert of pJC53.2 was used as negative control. All primer sequences used in cloning for RNAi experiments are listed in **table S2**.

Bulk RNAseq and data analysis:

Total RNA was extracted using the RNeasy Micro Kit (Qiagen) from single animals. Libraries were prepared using ~100 ng of total RNA as input using Universal Plus mRNA-Seq kit (Nugen) and sequenced on an Illumina Nextseq. Libraries were mapped to the dd_Smed_v6 transcriptome (*67*) using bowtie2 (*68*). Counts from the same isotigs were summed, and pairwise differential expression analysis was performed using DEseq2 (*69*). Normalized read counts from DESeq2 were scaled to generate z-scores for heatmaps.

Planarian cell dissociation:

10-15 mid-sized (~5-7 mm in length) asexual planarians were finely minced with a razor blade, suspended in CMF (Ca/Mg-Free media: 480 mg/L NaH_2PO_4, 960 mg/L NaCl, 1.44 g/L KCl, 960 mg/L $NaHCO_3$, 3.57 g/L HEPES, 0.24 g/L D-glucose, 1 g/L BSA, pH 7.4 in MilliQ H_2O), and rocked for 15 min with gentle pipetting for 10 times every 3 min until visibly homogenized. Cells were centrifuged at 400 × g for 5 min resuspended in 1 mL of fresh CMF, and serially filtered through 100, 70, 40 and 30-μm mesh strainers. After another spin, cells were resuspended in CMF supplemented with 1% BSA.

Cell lysis analysis *in vitro*:

For lysis assay, 50,000 cells were incubated overnight in 100 μL CMF supplemented with 1.5% FBS with control protein (h-CD8A) or ACT-2. Lysis was measured using Sony SH800 flow cytometry by the percentage of PI^+ cells. We observed that ACT-2 concentrations required to induce cell lysis were higher than typical physiological levels of signaling cues. This is likely due to the recombinant protein's lower biological activity compared to the endogenous proteins, as well as potential underestimates of *in vivo* concentrations, as local protein concentrations can be significantly higher than tissue-wide averages.

For cytoskeleton inhibition, the actin filament inhibitors, cytochalasin B (Cayman, Cat#11328), cytochalasin D (Cayman, Cat#11330), and latrunculin-A (Cayman, Cat#10010630), were added to the final concentrations of 60 μM, 60 μM and 7 μM, respectively.

To assess genotype specific responses, asexual and sexual cells were labeled with CFSE (Biolegend, Cat# 423801) or Celltrace Far Red (Invitrogen, Cat# 34564), respectively, and mixed at a 1:1 ratio with a total of 200,000 cells in 100 µL of CMF supplemented with 1.5% FBS.

For *E. coli* phagocytosis and dextran pinocytosis experiments, 50,000 total planarian cells were incubated overnight with 0.1 mg/mL pHrodo Green *E. coli* BioParticles (ThermoFisher Scientific, Cat# P35366) or 0.5 mg/mL Alexa Fluor 488-conjugated dextran (Invitrogen, Cat# D34682) in the presence of varying concentrations of ACT-2 proteins, with and without cytoskeleton inhibitors, in 100 µL CMF supplemented with 1.5% FBS. Flow cytometry was used to quantify phagocytosis and pinocytosis by gating for live cells with high fluorescence intensity indicating the uptake of *E. coli* or dextran.

FACS:

To isolate the ruptoblast population, dissociated cells were stained with Calcein Ultrablue AM (5 µM, AAT Bioquest, Cat# 21908) in CMF for 15 min at RT, washed, filtered, and incubated with PI (2 µg/mL) immediately before sorting on a Sony SH800 with a 130 µm chip. Cells were first gated for size using forward and back scattering, then based on Calcein Ultrablue and forward scattering (**Fig. 3C**, **fig. S5**). A total of ~450,000 cells were sorted into CMF supplemented with 1% BSA, and 1.5% FBS for single-cell RNAseq experiment, ~150,000 cells for time-lapse imaging, and ~300,000 cells each population for Western blots.

Time-lapse imaging:

For *in vitro* imaging, 96-well glass-bottom plates (Cellvis, Cat# P96-1-N) were coated with concanavalin A (50 μg/mL, Millipore, Cat# 11028-71-0) for 30 min. Approximately 50,000 cells were plated for 10 min before adding 20 μL of ACT-2 (10 μg/mL). Imaging began immediately on a Zeiss epifluorescence microscope using a EC Plan-Neofluar 10× objective (N.A = 0.3, working distance = 5.2 mm) or a LD Plan-Neofluar 63x objective (N.A = 0.75, working distance = 1.7 mm) at 2-12 frame/min. For imaging ruptoblast-mediated killing, P5 cells were labelled with CellTrace Violet (1:1,000, Invitrogen, Cat# C34571) and mixed 1:4 with unlabeled cells depleted of ruptoblasts (P1, P3, P4, P6).

For bacterial killing experiments, 96-well plates were coated with Poly-L-lysine (Cultrex, Cat#3438-100-01) for 30 min. 3 μL of *E. coli* (MG1655 attB::pproC-msfGFP, OD ~1.2) (*70*) were diluted in 60 μL of CMF and plated for 30 min. About 50,000 P5 cells in 100 μL of CMF with PI (2 μg/mL) were added and co-incubated 20 min prior to introducing 20 μL of ACT-2 (10 μg/mL) and proceeding to imaging. To quantify GFP^+ and PI^+ bacterial fractions, images were binarized using OpenCV and small debris were excluded by applying a minimum area threshold of > 10 pixels.

Single-cell RNAseq and data analysis:

Following FACS, 150,000 or 300,000 P5 cells were incubated for 5 min in CMF supplemented with 1% BSA containing either control protein (h-CD8A, 10 μg/mL) or ACT-2 (10 μg/mL), respectively. Cells were then centrifuged at 400 × g, resuspended in fresh CMF with the same protein for another 5 min, centrifuged again, and finally resuspended in CMF at ~1,000 cell/μL. Libraries were prepared using a 10x Genomics Chromium Controller with Chromium single cell

v3.1 library/Gel Bead Kit. Amplified cDNA libraries were quantified with a bioanalyzer and sequenced on an Illumina Novaseq S4 platform, generating in mean coverage of ~25,000 read pairs per cell.

UMI-tools (*71*) and cutadapt (*72*) were used for barcode tagging and adapter trimming, respectively. Reads were aligned to dd_Smed_v6 (*67*) transcriptome using bowtie2 with "–sensitive" parameters. Ambient RNA contamination was removed using SoupX (*73*) with default parameters. After removing low quality cells with fewer than 200 genes detected, we captured 1,500 genes and 4,000 UMI on average for the h-CD8A-treatedcontrol sample and 1,300 genes and 3,200 UMI for the ACT-2-treated sample. Counts were normalized such that each cell's total matched the median library size, and $\log_2$-transformed after adding a pseudo count of 1. Harmony (*74*) was used to integrate control and ACT-2 samples and SAM (*75*) was used for manifold reduction with default parameters, except for weight_mode = rms. Clusters were annotated based on known marker genes (*38*). Depletion factor was calculated as the ratio of relative abundance of each cluster in ACT-2 vs. control samples.

To identify ruptoblasts in the full planarian cell atlas and examine the specificity of their marker genes, we reanalyzed the published single-cell data (*38*) using the same pipeline, filtering out cells with <500 genes.

Identifying ruptoblasts across evolution:

Homologs of *fer3l-1* and downstream effectors including *ppib*, *ppibc*, *sspo*, *galnt* were identified via reciprocal BLAST, OrthoFinder (*76*) (run with default parameters) and EGGNOG (*77*). In

the nematode *C. elegans* and the cnidarians *H. vulgaris* and *N. vectensis*, no *fer3l-1* homolog was found. Using published single cell datasets, we found that *i*n *H. sapiens* (*78*) and the fly *D. melanogaster* (*79*), *fer3l-1* is expressed in neurons, whereas in the zebrafish *D. rerio* (*80*), *fer3l-1* is expressed minimally. In contrast, in the annelid *P. dumerilii* (*24*), marine flatworm *M. lignano* (*25*), and the acoel *H. miamia* (*23*), *fer3l-1* and its downstream effector genes are co-expressed in specific cell types, suggesting ruptoblast-like cells.

***Pseudomonas* infection:**

Pseudomonas isolated from the planarian (*26*) was inoculated in LB at 30 ^{o}C for 24 hr. OD600 was measured and converted to CFU/mL (*26*). Bacterial pellets were washed and resuspended in IO salts. Asexual animals (~3-4 mm in length) were washed several times before transferring to petri dishes containing bacteria. This process was repeated every 3 days.

Endogenous commensal bacterial quantification

Planarians (~3-4 mm in length) after RNAi were homogenized with 6 animals in 100 µL of milli-Q using a pestle, and the entire 100 µL was plated on LB agar without antibiotics. Plates were incubated in the dark at RT for 24 hr. A water-only control verified no contamination.

Supplementary Figures

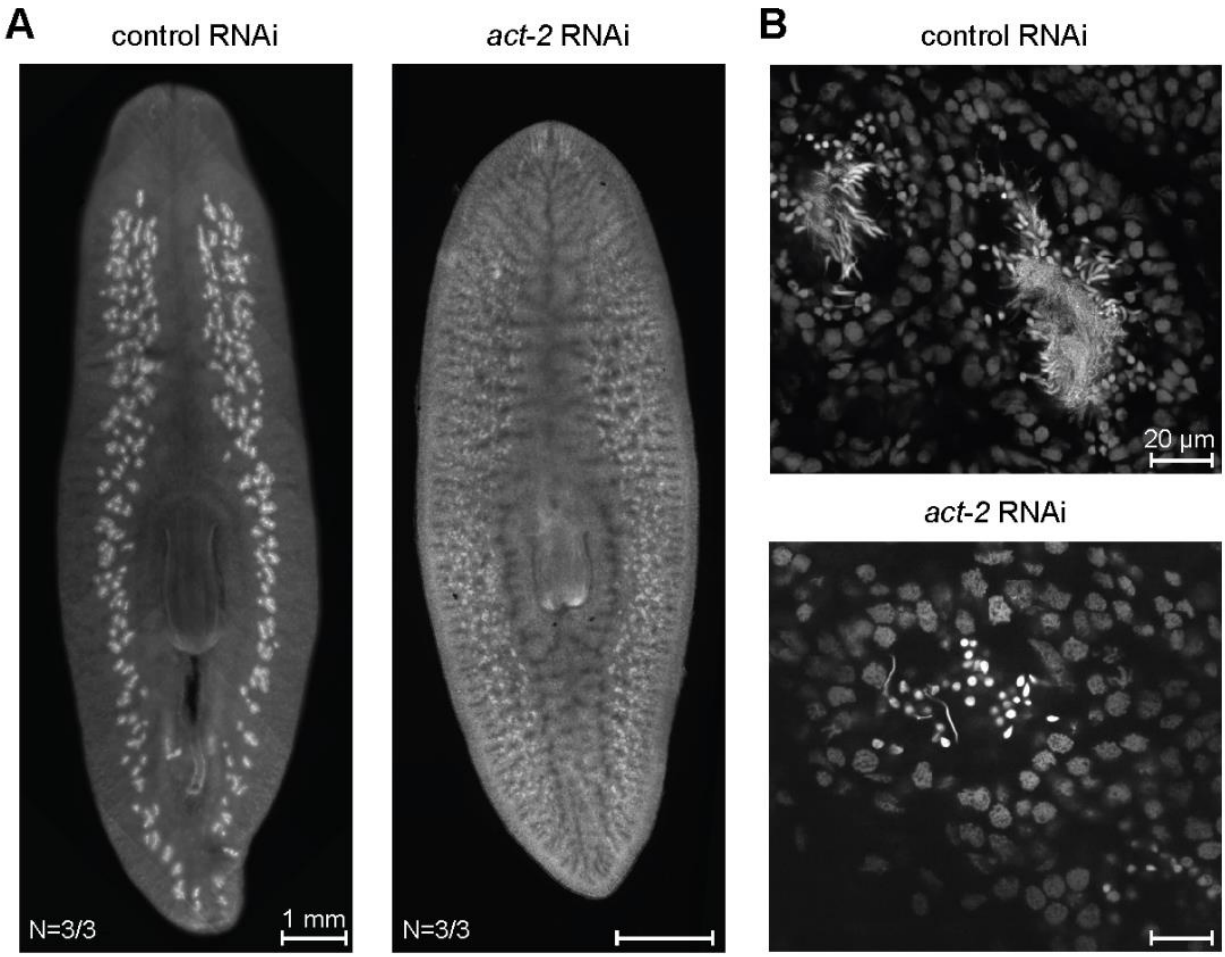

fig. S1. act-2 is required for spermatogenesis in sexual planarians.

(A) DAPI-stained testes of sexually mature planarians following 6 feedings of control or *act-2* RNAi. In control RNAi animals, large testes are distributed beneath the dorsal epithelium, whereas *act-2* RNAi animals exhibit only small clusters. N denotes the number of animals displaying the reported phenotypes out of total analyzed.

(B) Higher magnification imaging of testis lobules in control and *act-2* RNAi reveals defects in spermatogenesis. In controls, individual testis can be identified by the accumulation of sperm in the center of the lobule with a long, string-like morphology, surrounded by cells at various stages

of spermatogenesis. In contrast, testis lobules in *act-2* RNAi animals are smaller, largely devoid of differentiated cells across spermatogenic stages.

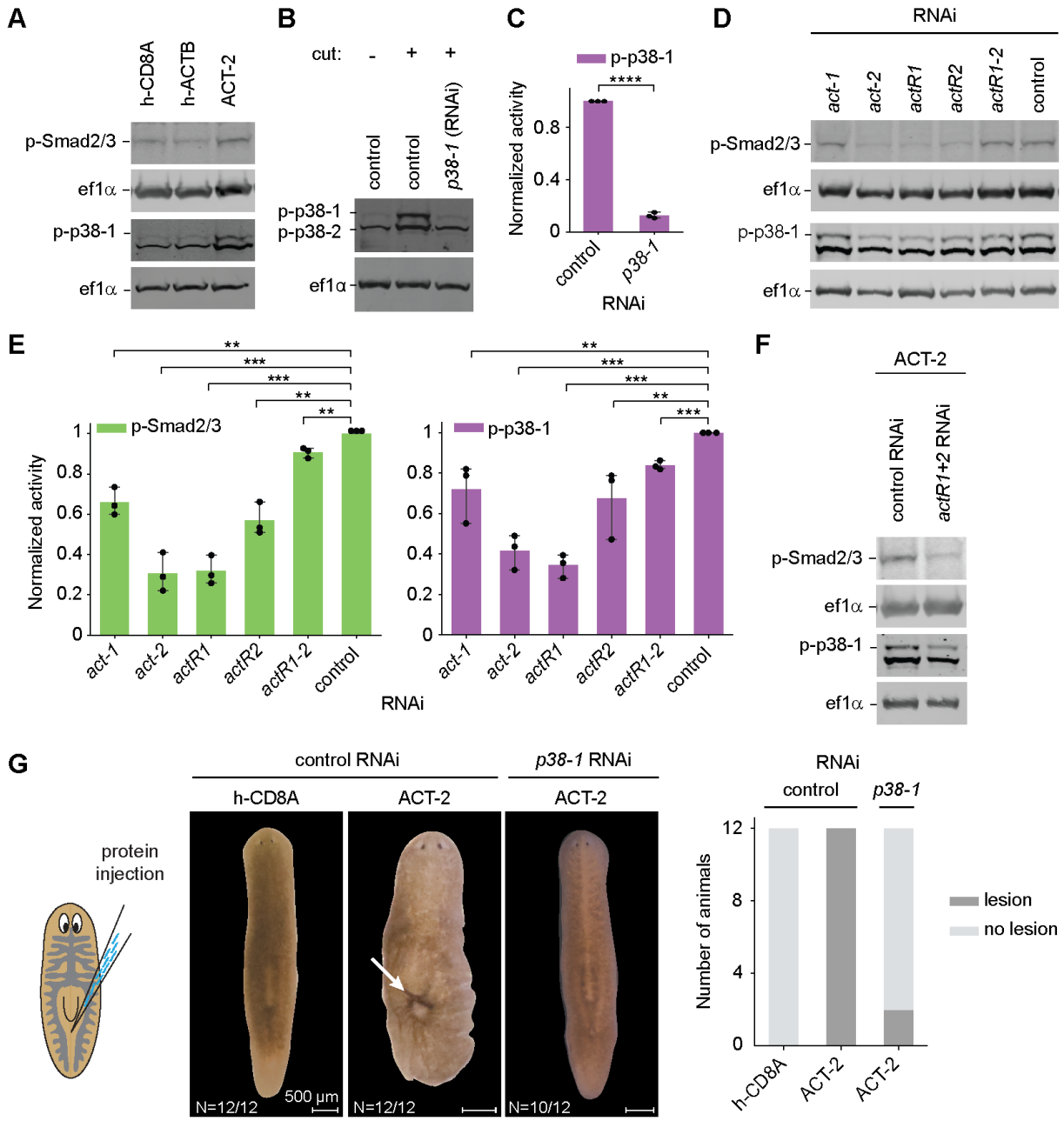

fig. S2. p38-1 is downstream of activin.

(A) Representative Western blotting images showing the increase of p-Smad2/3 and p-p38-1 in animals injected with ACT-2 proteins**,** but not control proteins (h-CD8A, h-ACTB). Quantification is shown in **Fig. 1C**.

(B-C) *p38-1* RNAi eliminates the p-p38-1 band after amputation, validating the specificity of the antibody. Note that amputation is used to activate p-38 as described in (*26*).

(D-E) Western blotting images (D) and quantification (E) showing that RNAi of the two activin homologs and three activin receptor homologs significantly reduce p-Smad2/3 (green) and p-p38-1 (magenta) levels. Quantified fold activation normalized to the levels in control RNAi animals. Statistical significance was determined by a two-sided t-test, error is reported as SD from three independent experiments, each containing five animals. $^{**}p < 0.01$, $^{***}p < 0.001$, NS, no significant difference.

(F) Representative Western blotting images for the quantification plot shown in **Fig. 1D**.

(G) (Left) Brightfield images of control RNAi animals injected with either control (h-CD8A) or ACT-2 protein, and *p38-1* RNAi-treated animals injected with ACT-2 protein. White arrow indicates lesions formed following injection. (Right) Number of animals with and without lesions across conditions.

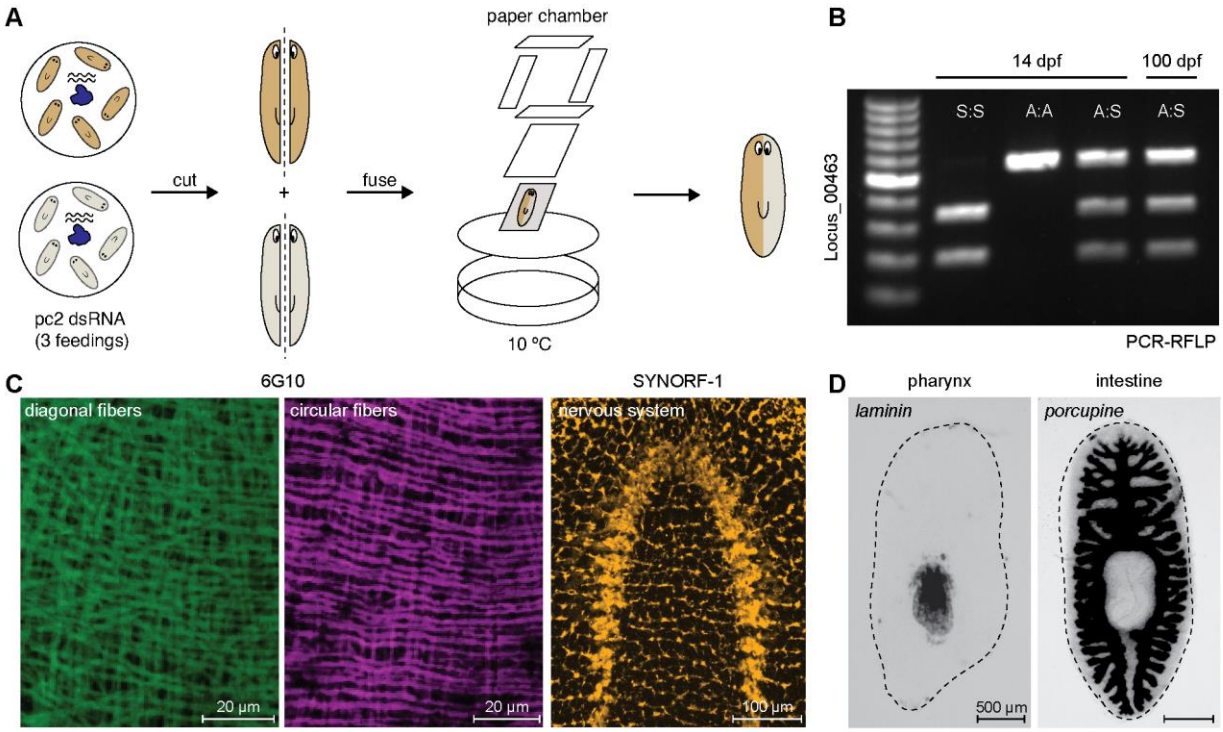

fig. S3. Complete tissue integration in genetic chimeras.

(A) Schematics showing the workflow of fusion experiments. Asexual and sexual animals are fed dsRNA against *pc2*, and the opposing halves are aligned and covered with Zig-Zag cigarette rolling paper. The fusion was further constrained by four pieces of filter paper, and a Kimwipe soaked with IO water to prevent drying.

(B) PCR-RFLP analysis of chimeras at 14 dpf and 100 dpf. Genotyping is based on locus 00463 cut by ScaI in sexual cells but not in asexual cells.

(C) Immunofluorescence showing complete structural integration of muscle fibers and neural tissue at the midline in chimeras at 20 dpf.

(D) WISH images of *laminin* (left) and *porcupine* (right) at 20 dpf illustrating the integration of pharynx and primary gut branches across the midline.

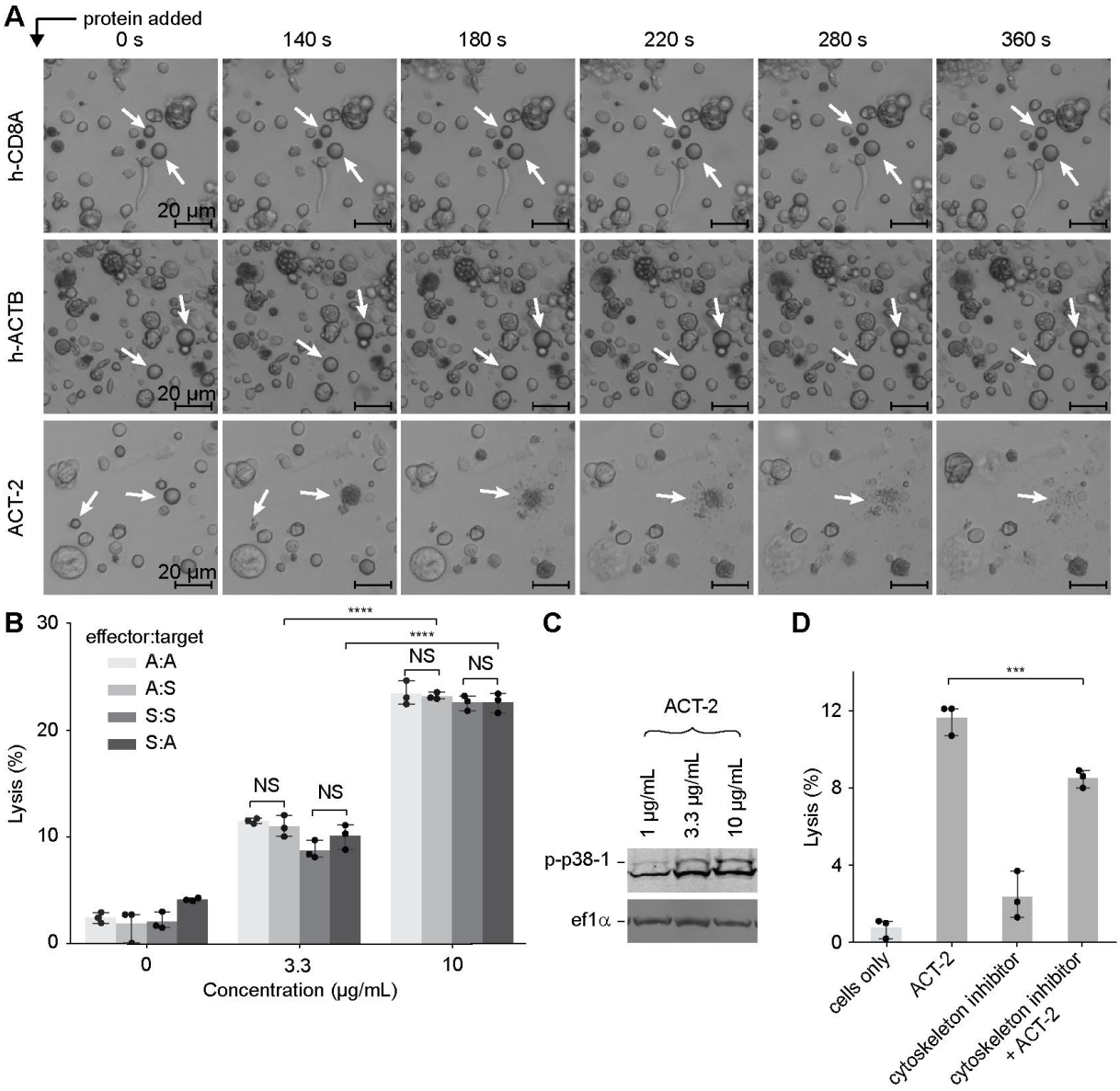

fig. S4. ACT-2 induces cell lysis regardless of the genotype.

(A) Snapshots showing cells undergoing explosive lysis only when incubated with 10 µg/mL ACT-2 proteins, but not with control proteins (h-CD8A or h-ACTB). White arrows indicate potential ruptoblasts based on morphology. The corresponding video is shown in **movie S1**.

(B) Flow cytometry analysis measuring PI^+ cells to assess lysis in response to distinct genotypes alone or in the presence of 3.3 or 10 µg/mL of ACT-2. Asexual and sexual cells were labeled

with CFSE or CellTrace Far Red, mixed at a 1:1 ratio (200,000 cells total), and analyzed across all labeling combinations. ACT-2 alone is sufficient to induce lysis.

(C) Representative Western blotting image for the quantification plot shown in **Fig. 3B**.

(D) Cell lysis measured in response to 10 μg/mL ACT-2 proteins with and without cytoskeleton inhibitor cocktails. Disruption of cytoskeleton integrity significantly reduced ACT-2 induced lysis.

Statistical significance in (B) and (D) was determined by a two-sided t-test, error was reported as SD from three independent experiments. ***$p < 0.001$, ****$p < 0.0001$, NS, no significant difference.

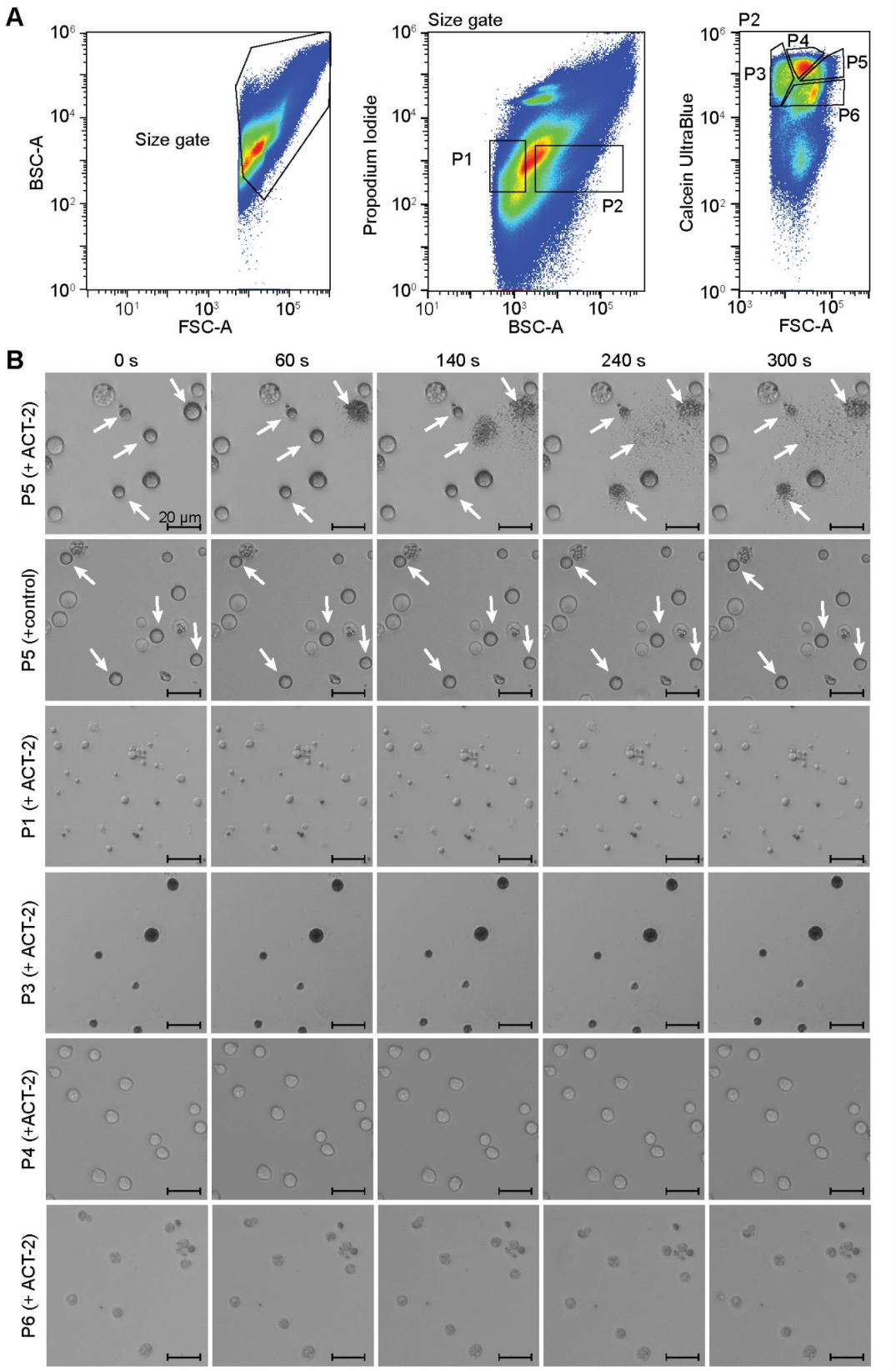

fig. S5. Sorting strategy to enrich for ruptoblasts.

(A) Flow cytometry gating strategy for sorting ruptoblasts. (Left) Initial gating based on size (Forward scatter: FSC) is used to eliminate debris and contaminants. (Middle) A second refinement step is performed using granularity (Back scatter: BSC), selecting live cells (PI^-) with medium-to-high BSC (P2) to exclude low-granularity cells (P1). (Right) P2 population is further subdivided into distinct subpopulations (P3, P4, P5, P6) based on Calcein UltraBlue intensity and FSC.

(B) Snapshot images of sorted subpopulations following exposure to 10 µg/mL ACT-2 protein. Live-imaging was used to refine the gating strategy and identify P5 as the only subpopulation responding to ACT-2. For a control, P5 subpopulation incubated with control protein (h-CD8A) do not undergo lysis. White arrows indicate potential ruptoblasts based on morphology. The corresponding video is shown in **movie S2**.

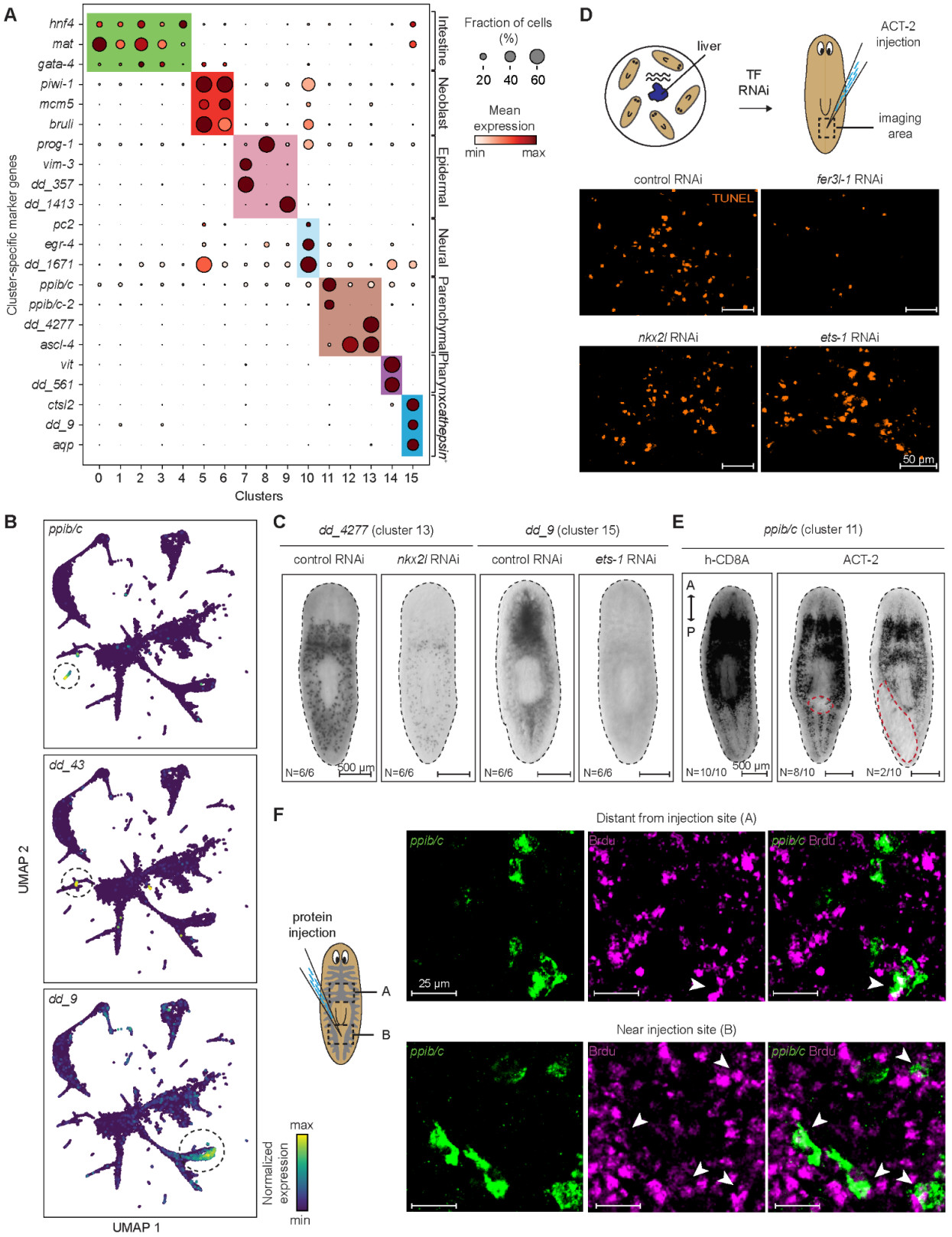

fig. S6. scRNAseq reveals molecular identity of ruptoblasts.

(A) Dotplot showing average expression of selected marker genes used in annotating cell type of the clusters. Contig numbers for all mentioned genes are listed in **table S3**.

(B) Marker gene expression of cluster 11, 13 and 15 overlaid on the UMAP projection of planarian cell atlas (*38*). Dashed circles indicate cells with high marker expression, demonstrating the specificity of these markers in the full atlas.

(C) WISH images showing the expression of *dd_4277* in control and *nkx2l* (*dd_13898*) RNAi (left) and *dd_9* in control and *ets-1* (*dd_2092*) RNAi (right) animals suggesting that knockdown of these TFs eliminate the corresponding cell populations. Dashed lines: animal outline.

(D) Representative images showing TUNEL$^+$ cells near the injection site for the quantification plot shown in **Fig. 4C** for control, *fer3l-1*, *nkx2l* and *ets-1* RNAi animals injected with ACT-2. Dashed box: imaging area.

(E) WISH images showing the elimination of *ppib/c*$^+$ cells (cluster 11) upon 10 μg/mL ACT-2 protein injection into the parenchymal tissue between posterior gut branches. Red dashed lines denote the region where cells have been removed, and black dashed lines indicate animal surface.

(F) Representative image of BrdU labelling (magenta) to detect newly differentiated ruptoblasts (BrdU$^+$/ *ppib/c*$^+$) at 5 dpi in regions distant from and near the injection sites. Corresponding quantification plot is shown in **Fig. 4F.**

In (C) and (E), N denotes the number of animals consistent with the images out of the total number of animals analyzed.

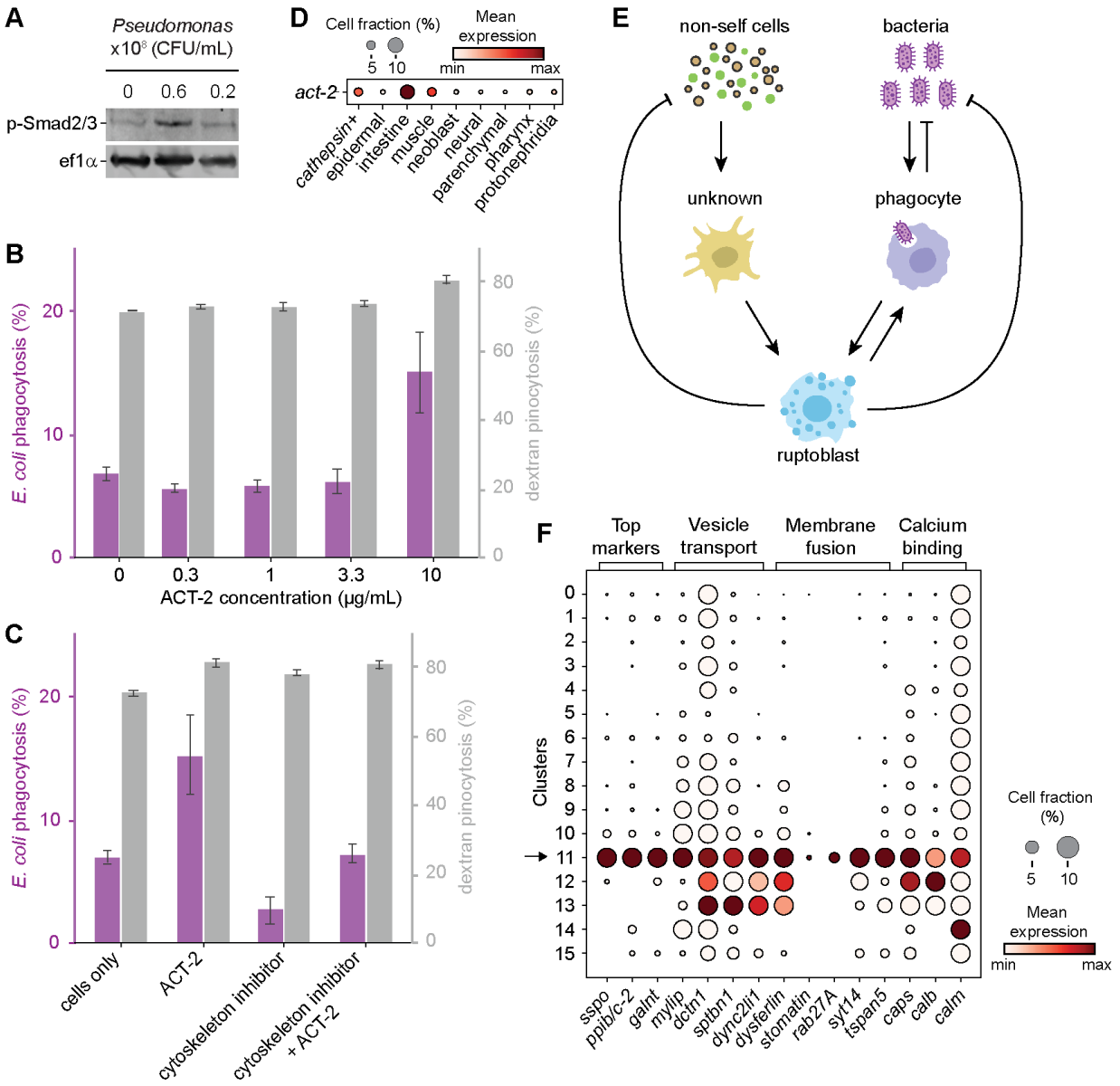

fig. S7. Ruptoblasts operate within a broad immune network.

(A) Representative Western blotting image for the quantification shown in **Fig. 5B.**

(B-C) Quantification of phagocytosis and pinocytosis of unsorted total cells in response to ACT-2. Phagocytosis of pHrodo Green *E. coli* bioparticles (magenta) and pinocytosis of dextran (grey) were measured following treatment with varying concentrations of ACT-2 protein in (B) and 10

μg/mL of ACT-2 with and without cytoskeleton inhibitor cocktails in (C). Error bars represent standard deviation (SD) from three independent experiments, each containing 50,000 cells.

(D) Dotplot showing mean expression of act-2 in major cell types in the planarian cell atlas (*39*).

(E) Schematics showing the immune network in which ruptoblasts are activated by cells that detect non-self genotypes or by phagocytes that engulf bacteria, triggering a pro-inflammatory cascade with ruptoblasts eliminating non-self cells or bacteria. Ruptolasts also provide feedback to phagocytes, potentially enhancing their activity to clear bacteria and debris.

(F) Dotplot showing expression of top marker genes, vesicle transport motor proteins, regulators of membrane fusion, docking, exocytosis and calcium binding proteins in ruptoblasts (cluster 11) indicated by the arrow. Contig numbers for all mentioned genes are listed in **table S3**.

Supplementary Tables

table S1. Summary of previously characterized cell death processes, outlining their key cellular events, timescales and molecular regulators that are different from ruptosis.

Cell death or killing mode	*Features distinct from ruptosis*	*Time scale*	*Key components*	*Expression in ruptoblast*	*Kill?*	*Ref*
necroptosis	nuclear intact, no degranulation	hours	RIPK1/3, MLKL	none	no	81,82,83
pyroptosis	nuclear intact, chromatin condensation, pore-induced intracellular traps	minutes-hours	caspase-1, GSDMD	none	no	82,83
ferroptosis	nuclear intact, no degranulation, iron-dependent membrane lipid oxidation	hours	iron	none	no	83,84
parthanatos	no degranulation, nuclear condensation, production of poly (ADP-ribose), release of mitochondrial apoptosis inducing factor	hours	poly (ADP-ribose) polymerase 1	none	no	85
MPT-driven necrosis	nuclear intact, mitochondrial permeability transition, pore opening and swelling	minutes-hours	cyclophilin D (PPIF), voltage dependent anion channel	none	no	83,86
suicidal NETosis	chromatin decondensation, release of extracellular traps	hours	PAD4, serine protease, gasdermin D, calpain-dependent	none	yes	48,49
vital NETosis	release of extracellular traps, no membrane rupture	minutes-hours	NOX-dependent pathway	none	yes	48,49
neutrophil degranulation	no membrane rupture	minutes	p38, GTPase, SNARE	p38, GTPase	yes	20

table S2. List of primer sequences used in cloning for in-situ hybridization and RNAi experiments.

table S3. List of gene IDs associated with planarian genes used throughout the study.

Supplementary Movies

movie S1. Brightfield time-lapse videos of total planarian cells incubated with 10 μg/mL of control proteins (h-CD8A or h-ACTB) or ACT-2 protein. Proteins are added at 0s. Time stamp: minute:second.

movie S2. Brightfield time-lapse videos of sorted subpopulations (P1, P3–P6) incubated with 10 μg/mL ACT-2 proteins. Only P5 responds to ACT-2. As a comparison, P5 incubated with 10 μg/mL control (h-CD8A) protein is shown to demonstrate the absence of lysis. ACT-2 and h-CD8A proteins are added at 0 s. Time stamp: minute:second.

movie S3. Brightfield time-lapse video of a ruptoblast undergoing ruptosis upon activation with 10 μg/mL of ACT-2. ACT-2 is added at 0 s. Time stamp: minute:second.

movie S4. Time-lapse video of a ruptoblast labeled with CellTrace Violet (blue) killing nearby unlabeled cells, as indicated by PI (red) uptake. ACT-2 is added at 90 s. Time stamp: minute:second.

movie S5. Time-lapse video showing a ruptoblast killing nearby *E. coli* upon activation by 10 μg/mL ACT-2, as indicated by the loss of cytoplasmic GFP (green) followed by PI uptake (red). As a control, P4 subpopulation incubated with *E. coli* along with 10 μg/mL ACT-2 is shown, demonstrating the absence of bacterial lysis. ACT-2 is added at 0 s. Time stamp: minute:second.